MEASURING ELASTIC CONSTANTS OF LAMINATED COPPER/NIOBIUM COMPOSITES USING RESONANT ULTRASOUND SPECTROSCOPY

by

KEVIN GALIANO

Submitted to the Department of Physics
in partial fulfillment of the requirements for the degree of
BACHELOR OF SCIENCE
at the
MASSACHUSETTS INSTITUTE OF TECHNOLOGY
June 2013

Author .....
Department of Physics
May 28, 2013

Certified by..
Michael J. Demkowicz
Assistant Professor of Materials Science and Engineering
Thesis Supervisor

Certified by.....
Raymond Ashoori
Professor of Physics
Thesis Supervisor

Accepted by .....
Professor Nergis Mavalvala
Senior Thesis Coordinator, Department of Physics

MEASURING ELASTIC CONSTANTS OF LAMINATED COPPER/NIOBIUM COMPOSITES USING RESONANT ULTRASOUND SPECTROSCOPY

by

KEVIN GALIANO

Submitted to the Department of Physics
on May 28, 2013, in partial fulfillment of the
requirements for the degree of
BACHELOR OF SCIENCE

Abstract

Layered copper/niobium (Cu/Nb) composites with small layer widths contain a high area per unit volume of solid-state interfaces. Interfaces have their own elasticity tensor, which affects the elastic properties of the composite as a whole. We have studied the elastic constants of Cu/Nb composites with different layer thicknesses with a view to determining the elastic constants of Cu/Nb interfaces. Our work relied on resonant ultrasound spectroscopy (RUS): a technique for deducing elastic constants from measured resonance frequencies. Resonance frequencies of three samples with differing layer widths were measured. A numerical approach for matching measured and computed resonance frequencies was developed and used in deducing the elastic constants of the composite. The uncertainties in the elastic constants thereby obtained were too large to estimate interface elastic properties. However, several sources of this uncertainty were identified, paving the way to improved elastic constant measurements in the future.

Thesis Supervisor: Michael J. Demkowicz
Title: Assistant Professor of Materials Science and Engineering

Thesis Supervisor: Raymond Ashoori
Title: Professor of Physics

Acknowledgments

This work involved the help and collaboration of many people. The author is grateful to Dr. Michael Demkowicz and Dr. Raymond Ashoori (MIT) for supervising the development of this thesis. The author is also grateful to Dr. Nicolás Mujica and Dr. Fernando Lund (University of Chile) for having provided the opportunity to join and take part in their lab group. Dr. Mujica and Dr. Lund provided us with the experimental equipment for conducting RUS measurements. Dr. Mujica also provided us with the idea of developing a numerical approach for the mode identification. The author also appreciates the help of Domingo Jullian, Carolina Espinoza Oñate, and María Teresa Cerda Guevara (University of Chile) for their valuable discussions and help involving the implementation of RUS. Our samples were prepared by our collaborators at Los Alamos National Laboratory who performed the accumulated roll bonding procedure for us.

In the part of the development of RUS codes, the author also received help from several people. Dr. Paul Heyliger (Colorado State University) provided email discussions involving the use of the interpolation basis. Dr. Albert Migliori (LANL) also provided us with his source code for the fitting routine in RUS. Dr. Julien Langou (UCDenver) provided email support about the implementation of the LAPACK libraries. Richard Baumer (MIT) helped considerably with the compilation of libraries for the eigenvalue routines in RUS. Scott Skirlo (MIT) provided help for the calculation of effective elastic constants. Finally, Dr. Carlos Tomé (LANL) provided us with his VPSC code and multiple email conversations regarding the calculation of polycrystalline elastic constants of copper and niobium.

All of these people provided valuable help in the development of this thesis and the author appreciates the time each one of them provided.

Contents

List of Figures

List of Tables

Chapter 1

Introduction

1.1 Motivation for Studying Layered Copper/Niobium Composites

Our work is on composites, which are materials composed of 2 or more constituents. We focus on composites with a specific morphology and composition, namely on layered composites of copper (Cu) and niobium (Nb). Fig. 1-1 shows a schematic illustrating the morphology of these composites.

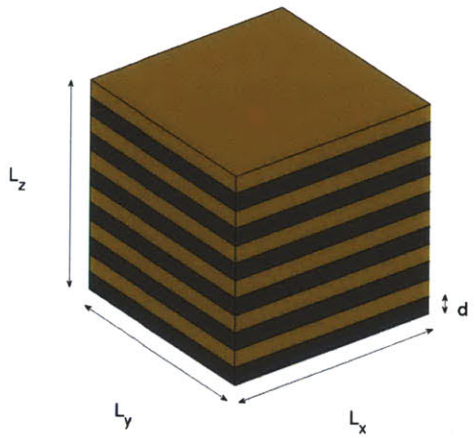

Figure 1-1: A layered Cu/Nb composite. Cu layers are shown in brown while Nb layers are shown in gray. This diagram is not drawn to scale, as the layer thickness d is much smaller than the lateral dimensions in the samples we studied.

Layered Cu/Nb composites contain numerous interfaces between neighboring

Cu/Nb layers. These interfaces have physical properties of their own, distinct from the properties of pure Cu and Nb. For example, previous experiments have suggested that Cu/Nb interfaces have their own, unique elastic constants [1]. However, these studies used techniques such as Brillouin scattering, which do not give the complete elastic constant tensor. The motivation of our work was to measure the full elastic constant tensor of Cu/Nb interfaces using resonant ultrasound spectroscopy (RUS). To the best of our knowledge, our work is the first application of RUS to layered composites.

The influence of interfaces on the elastic properties of the composite is proportional to the ratio between the total interface area and the volume of the sample. If we define the number of interfaces in the sample to be N, then the total interface area is

$$A_{\text{interfaces}} = NL_xL_y. \tag{1.1}$$

The volume of the sample is $L_xL_yL_z$. If we define d to be a constant layer width, then the volume can be expressed as

$$V = (N+1)L_xL_yd. \tag{1.2}$$

Thus, when the number of interfaces is large, the interface area-to-volume ratio scales as $1/d$:

$$\lim_{N\to+\infty} \frac{A_{\text{interfaces}}}{V} = \lim_{N\to+\infty} \frac{NL_xL_y}{L_xL_yL_z} = \lim_{N\to+\infty} \frac{N}{(N+1)d} = \frac{1}{d} \tag{1.3}$$

As the layer width decreases, the interface area-to-volume ratio increases and the influence of the interfaces becomes larger. Thus, it may be possible to determine interface elastic constants by measuring the total elastic constants of several layered composites with differing layer thicknesses, provided that the interface area-to-volume ratio of all the composites is sufficiently large. In practice, layer thicknesses in the range of several nanometers to several tens of nanometers are required.

Interface elastic constants may influence several physical properties of technological importance, such as composite thermal conductivity, which is of great importance

for the development of highly efficient thermoelectrics for clean energy applications. Interfaces also play an important role in the mechanical- and radiation-response of layered composites. For example, Cu/Nb composites with layer thicknesses of 700 nm or less have been found to be stronger than what is expected from the rule of mixtures [2]. This effect results from the interaction of dislocations with interfaces, which depends on interface elastic constants. Cu/Nb composites with low layer thicknesses have been also been found to be radiation resistant [3]. This unusual behavior is also attributable to interfaces, specifically interactions between interfaces and radiation-induced point defects. Such interactions are also sensitive to interface elastic properties.

While RUS has important advantages, many difficulties arise in its application to composites. Although our original goal was to characterize the elastic constants of Cu/Nb interfaces, we did not achieve this because of several problems or difficulties that we encountered. However, we identified several potential sources of these difficulties, providing a path to improving future RUS measurements. We discuss more about these topics in Chapters 3, 4, and 6 and also in the conclusions.

1.2 Elastic Constants

When a material is deformed, its shape and its dimensions can change. The strain tensor, ϵ_{ik} , provides the length change per unit length at a given point.

$$\epsilon_{ik} = \frac{1}{2}\left(\frac{\partial u_i}{\partial x_k} + \frac{\partial u_k}{\partial x_i}\right) \tag{1.4}$$

The indices can vary from 1 to 3, corresponding to a 3-dimensional body, and u_i corresponds to the change in length Δx_i that occurs during the deformation. The stress tensor σ_{ij} characterizes the force F_i that acts upon a given area or surface A_j of a body.

$$F_i = \sigma_{ij} A_j \tag{1.5}$$

The elastic constants tensor C_{ijkl} can be used to characterize the elastic response of materials.[4]

$$\sigma_{ij} = C_{ijkl}\epsilon_{kl} \tag{1.6}$$

The elasticity tensor contains 81 elements. We can show this rank 4 tensor using the notation in Mathematica as follows.

$$C_{ijkl} = \left(\begin{array}{ccc|ccc|ccc} C_{1111} & C_{1112} & C_{1113} & C_{1211} & C_{1212} & C_{1213} & C_{1311} & C_{1312} & C_{1313} \\ C_{1121} & C_{1122} & C_{1123} & C_{1221} & C_{1222} & C_{1223} & C_{1321} & C_{1322} & C_{1323} \\ C_{1131} & C_{1132} & C_{1133} & C_{1231} & C_{1232} & C_{1233} & C_{1331} & C_{1332} & C_{1333} \\ \hline C_{2111} & C_{2112} & C_{2113} & C_{2211} & C_{2212} & C_{2213} & C_{2311} & C_{2312} & C_{2313} \\ C_{2121} & C_{2122} & C_{2123} & C_{2221} & C_{2222} & C_{2223} & C_{2321} & C_{2322} & C_{2323} \\ C_{2131} & C_{2132} & C_{2133} & C_{2231} & C_{2232} & C_{2233} & C_{2331} & C_{2332} & C_{2333} \\ \hline C_{3111} & C_{3112} & C_{3113} & C_{3211} & C_{3212} & C_{3213} & C_{3311} & C_{3312} & C_{3313} \\ C_{3121} & C_{3122} & C_{3123} & C_{3221} & C_{3222} & C_{3223} & C_{3321} & C_{3322} & C_{3323} \\ C_{3131} & C_{3132} & C_{3133} & C_{3231} & C_{3232} & C_{3233} & C_{3331} & C_{3332} & C_{3333} \end{array}\right) \tag{1.7}$$

Due to symmetries of the tensor, the maximum number of independent elastic constants that a material can have is 21. In order to simplify the rank 4 tensor, we can represent it using the rank 2 matrix convention which we show in Table 1.1.

Table 1.1: The convention for converting 2 indices of an element of the elasticity tensor to 1 index of the matrix form is presented. This table was adapted from [4].

Tensor Indices	11	22	33	23,32	31,13	12,21
Matrix Indices	1	2	3	4	5	6

In a material with orthotropic symmetry, several of the terms vanish and there are only 9 independent elastic constants.

$$C_{ijkl}^{\text{orthotropic}} = \left(\begin{array}{ccc} \begin{pmatrix} C_{11} & 0 & 0 \\ 0 & C_{12} & 0 \\ 0 & 0 & C_{13} \end{pmatrix} & \begin{pmatrix} 0 & C_{66} & 0 \\ C_{66} & 0 & 0 \\ 0 & 0 & 0 \end{pmatrix} & \begin{pmatrix} 0 & 0 & C_{55} \\ 0 & 0 & 0 \\ C_{55} & 0 & 0 \end{pmatrix} \\ \begin{pmatrix} 0 & C_{66} & 0 \\ C_{66} & 0 & 0 \\ 0 & 0 & 0 \end{pmatrix} & \begin{pmatrix} C_{21} & 0 & 0 \\ 0 & C_{22} & 0 \\ 0 & 0 & C_{23} \end{pmatrix} & \begin{pmatrix} 0 & 0 & 0 \\ 0 & 0 & C_{44} \\ 0 & C_{44} & 0 \end{pmatrix} \\ \begin{pmatrix} 0 & 0 & C_{55} \\ 0 & 0 & 0 \\ C_{55} & 0 & 0 \end{pmatrix} & \begin{pmatrix} 0 & 0 & 0 \\ 0 & 0 & C_{44} \\ 0 & C_{44} & 0 \end{pmatrix} & \begin{pmatrix} C_{31} & 0 & 0 \\ 0 & C_{32} & 0 \\ 0 & 0 & C_{33} \end{pmatrix} \end{array}\right) \tag{1.8}$$

We can represent this in the following matrix form.

$$C_{ij}^{\text{orthotropic}} = \begin{pmatrix} C_{11} & C_{12} & C_{13} & 0 & 0 & 0 \\ C_{21} & C_{22} & C_{23} & 0 & 0 & 0 \\ C_{31} & C_{32} & C_{33} & 0 & 0 & 0 \\ 0 & 0 & 0 & C_{44} & 0 & 0 \\ 0 & 0 & 0 & 0 & C_{55} & 0 \\ 0 & 0 & 0 & 0 & 0 & C_{66} \end{pmatrix} \tag{1.9}$$

In our fitting procedures we have worked with cubic systems that contain 3 independent elastic constants.

$$C_{ij}^{\text{cubic}} = \begin{pmatrix} C_{11} & C_{12} & C_{12} & 0 & 0 & 0 \\ C_{12} & C_{11} & C_{12} & 0 & 0 & 0 \\ C_{12} & C_{12} & C_{11} & 0 & 0 & 0 \\ 0 & 0 & 0 & C_{44} & 0 & 0 \\ 0 & 0 & 0 & 0 & C_{44} & 0 \\ 0 & 0 & 0 & 0 & 0 & C_{44} \end{pmatrix} \tag{1.10}$$

Many of our simulations implement isotropic materials that contain only 2 independent elastic constants, and they have the constraint, $C_{12} = C_{11} - 2C_{44}$.

$$C_{ij}^{\text{isotropic}} = \begin{pmatrix} C_{11} & C_{11}-2C_{44} & C_{11}-2C_{44} & 0 & 0 & 0 \\ C_{11}-2C_{44} & C_{11} & C_{11}-2C_{44} & 0 & 0 & 0 \\ C_{11}-2C_{44} & C_{11}-2C_{44} & C_{11} & 0 & 0 & 0 \\ 0 & 0 & 0 & C_{44} & 0 & 0 \\ 0 & 0 & 0 & 0 & C_{44} & 0 \\ 0 & 0 & 0 & 0 & 0 & C_{44} \end{pmatrix} \tag{1.11}$$

1.3 Description of Resonant Ultrasound Spectroscopy

Resonant ultrasound spectroscopy (RUS) is an experimental technique that was developed by Migliori and co-workers [5]. It provides many advantages over the other techniques as RUS can be used to determine the complete elasticity tensor with a single measurement. It can be implemented in a large temperature range, and it is generally not limited by the geometry of the sample.[6]

RUS relies on measurements of resonance frequencies to determine elastic constants. Thus, RUS is a non-destructive technique. However, it does not measure elastic properties directly. Rather, these must be deduced by interpreting measure-

ments of resonant frequencies. This is accomplished using a numerical calculation of resonance frequencies given a set of trial elastic constants (the "direct code"). The trial elastic constants are then adjusted until the calculated and measured resonance frequencies match. A special "inverse code" is developed to automate the fitting procedure. A flowchart with the stages of a RUS measurement is presented in Fig. 1-2.

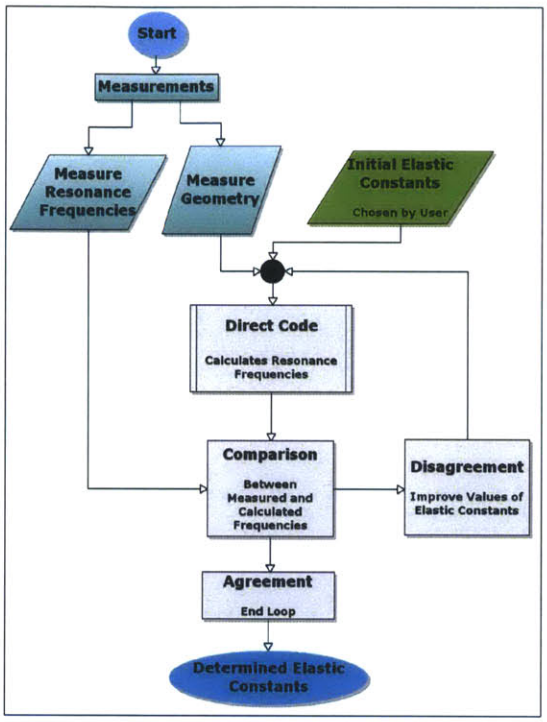

Figure 1-2: Flowchart of the some of the steps involved in using RUS to determine the elastic constants of a sample.

RUS can be used to measure the elastic constants of a material with any kind of symmetry (isotropic, cubic, transverse, etc). It could even be implemented using a set of 21 independent elastic constants and the runtime of the direct code would be practically unaffected. However, as the system becomes less symmetric, the inverse code generally requires more time to fit for the elastic constants.

Chapter 2 describes the experimental background on RUS and how the measurements are conducted. In Chapter 3 we discuss the "direct code" along with simulations we performed to validate it. In Chapter 4 we have also developed a numerical approach to match measured and calculated resonance frequencies. Chapter 5 dis-

cusses the implementation of the "inverse code" to determine elastic constants. In Chapter 6 we present data that we have collected from 3 Cu/Nb samples. We discuss several attempts to deduce elastic constants of Cu/Nb laminates from this data. Finally, in Chapter 7 we summarize the obstacles and uncertainties we have encountered as well as some of the advancements we have achieved through this work.

Chapter 2

Experimental Technique of RUS

2.1 Information on Samples

We have 4 layered Cu/Nb samples with different layer widths, d. We present the information about these samples in Table 2.1. Our collaborators at Los Alamos National Laboratory prepared these samples for us using the technique of accumulated roll bonding (ARB). This technique allows for the preparation of samples with a large interface area-to-volume ratio.

The pictures shown in Table 2.1 do not correspond to the exact samples which we used in our experiments. Initially, the 4 samples arrived at larger sizes. We used electric discharge machining to cut each sample to a smaller size. We based these cuts on simulations we made to estimate the number of available resonances and we also sought to obtain samples that were uniform in their geometry. As a result of this, we had more than one copy of each sample at each layer width.

However, there is a problem with ARB when the layer width becomes very small as it can cause damage to the sample in the form of fractures. Such damage can be visible in the picture of sample 4, the one with the smallest layer width at 7.5 nm. This damage impedes the geometry from being uniform. According to [6], inhomogeneities in the geometry can cause the composite function in the fitting routine to become shallow and they can generate multiple minima. Because of this, we have decided to not analyze data from sample 4.

Table 2.1: Four ARB samples were prepared by our collaborators at LANL. We present their geometry with pictures showing the xy plane of three of the samples at two different magnifications. Terms in brackets correspond to values that were provided to us by our collaborators at Los Alamos. The thickness L_z is in units of μm. All other unlabeled quantities are in cgs units.

	Sample 1	Sample 2	Sample 3	Sample 4
[Layers]	12	8160	16320	34680
M	10.3074 ± 0.0001	0.8150 ± 0.0002	0.6660 ± 0.0001	0.6956 ± 0.0001
L_x	2.5022 ± 0.0008	3.161 ± 0.001	2.8408 ± 0.0004	3.219 ± 0.002
L_y	2.4014 ± 0.0005	1.006 ± 0.001	1.0036 ± 0.0005	1.002 ± 0.002
L_z	1975 ± 7	300.2 ± 1.5	273.8 ± 0.8	260.4 ± 2.6
d	164.6 μm	36.79 nm	16.78 nm	7.509 nm
ρ	8.685	8.537	8.532	8.282
$[L_z]$		279 μm	254 μm	254 μm
$[d]$		34.191 nm	15.564 nm	7.3241 nm
$[\rho]$		9.186	9.197	8.491
Low				
High				

It is interesting to note that in samples 2 and 3, the densities are nearly the same. This is consistent with what is expected, because ARB samples with large interface area-to-volume ratio tend to have constant layer widths.

2.2 Experimental Setup

In RUS, a piezoelectric actuator is used excite elastic vibrations in a solid specimen over a range of frequencies while another piezoelectric transducer measures the resonances. A schematic of our experimental setup is shown in Fig. 2-1. The goal is to try to minimize contact between the sample and the experimental setup, because a greater contact force can cause the resonances to shift from their original frequencies. To improve this, the setup includes a set of springs and an air compressor (not shown) to reduce the friction. The height of the piezoelectric transducer is adjustable.

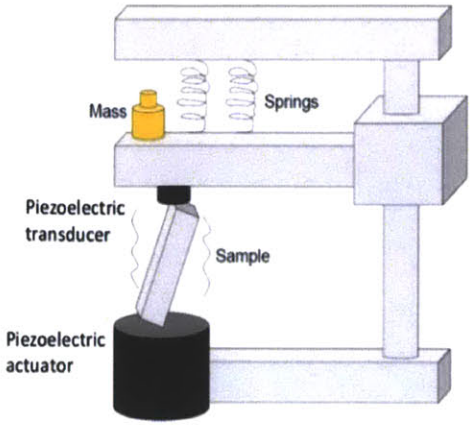

Figure 2-1: A piezoelectric actuator is used excite elastic vibrations in a solid specimen over a range of frequencies while a transducer measures the deformation response.

Before the sample is placed on the actuator, the transducer height is raised until it is just above the sample. Then, the sample is placed and small masses are added next to the springs until the transducer begins to come in contact with the sample. Once the sample is in place, the deformation response of the sample can be measured as a function of frequency.

2.3 Measurement Techniques

The resonant spectrum that is obtained from RUS contains a series of peaks that correspond to the resonance frequencies. We present a sample spectrum in Fig. 2-2.

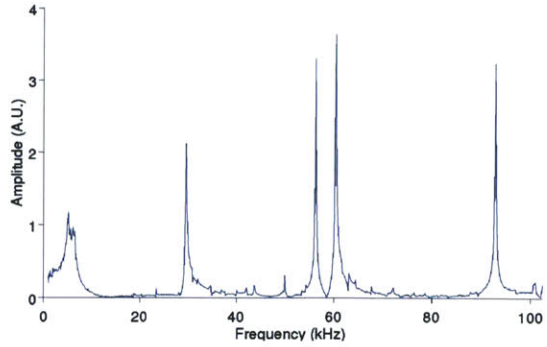

Figure 2-2: A resonant spectrum from sample 2 is presented. The voltage source that was applied to the actuator was 70 mV.

One of the problems that tends to occur when RUS measurements are conducted is that certain modes can have a node at a corner, causing them to have very little amplitude in the resonant spectra, and this can lead to them being missed. While it is often possible to make a peak become more visible by increasing the voltage source that is applied to the piezoelectric actuator, this can also result in the resonances entering the nonlinear elasticity regime. For this, it is important to identify a range where the elastic response is still linear.

There are multiple approaches for identifying when the system is entering the nonlinear elasticity regime. One approach is to collect multiple spectra, applying a different voltage source each time, and to normalize each spectra according to their respective voltage sources. If the normalized spectra are graphed together, they should stack on top of each other while the system is in the linear regime. We present this in Fig. 2-3. The spectra at lower voltage sources (blue) is more noisy than the spectra at higher voltage sources (red). However, with increasing voltage source, there is a shift in the resonance frequency.

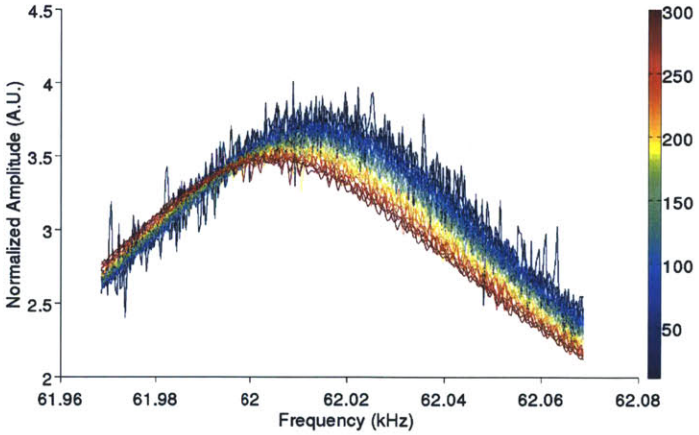

Figure 2-3: Multiple spectra of the resonant response at about 62 kHz of sample 3 are presented. The spectra are color-coded according to the voltage source which is in units of mV.

Another approach is to measure the resonance frequency as a function of increasing voltage source, and look for this systematic shift. In Fig. 2-4, at higher voltage sources there is a systematic decrease in resonance frequency which is consistent with the

leftward movement of the peak in Fig. 2-3.

A third approach is to graph the peak amplitude (deformation response) as a function of voltage source and look for a loss of linearity in the curve. We present this in Fig. 2-5. In this case, curve still appears to be linear, despite our other observations.

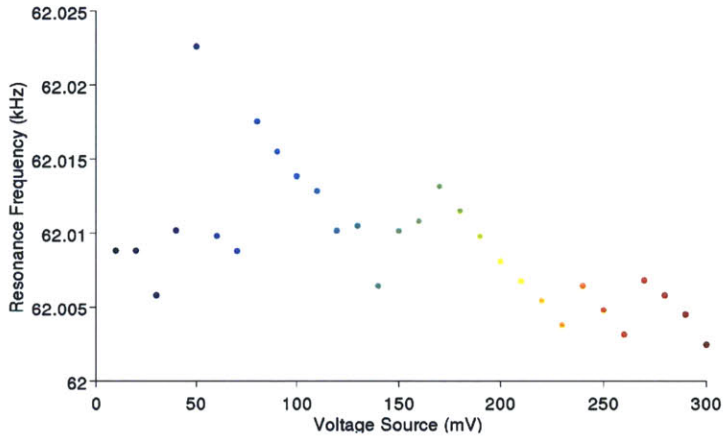

Figure 2-4: A graph of the resonance frequency of the peak near 62 kHz of Sample 3 is presented as a function of voltage source.

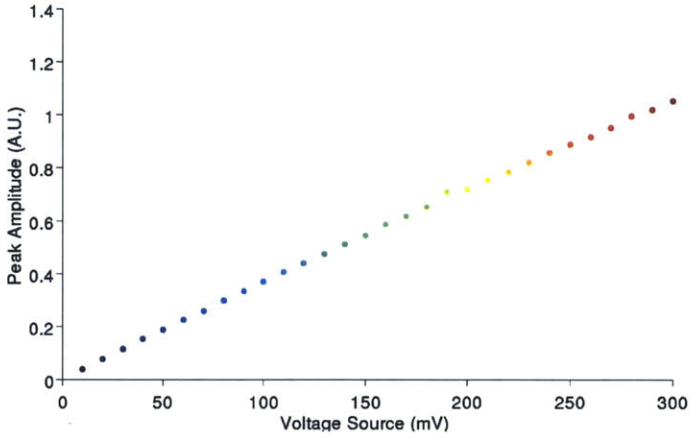

Figure 2-5: A graph of the peak amplitude of the resonance near 62 kHz of Sample 3 is presented as a function of voltage source.

Based on the results from Fig. 2-3 and 2-4, we assigned the linear regime to include voltage sources up to about 130 mV. At that point, the resonance frequency is still close to its values at very low voltage sources (below 50 mV).

Chapter 3

Theory of the Direct Code in RUS

The direct code is used to calculate the resonance frequencies of a sample, given its geometry and a set of input elastic constants. The process we use to derive the eigenvalue equation is the same for both homogeneous and layered samples, while the process of calculating matrix elements changes. We conduct simulations with both homogeneous and layered samples using both power series and interpolation baseses. These simulations have led us to find interesting applications that we present in Section 3.4.3 for working with layered samples with large interface area-to-volume ratio.

3.1 The Eigenvalue Equation

To calculate the resonance frequencies of the sample, we can begin with the Lagrangian, L, that can be defined in terms of the kinetic energy density, K, and the elastic potential energy density, U.

$$L = \int_V (K - U) dV \tag{3.1}$$

When a vibrational mode of the system is excited, the particles of the sample are displaced from their stationary positions. We refer to this displacement as $\vec{u}$ with components u_i where i ranges from 1 to 3. This corresponds to displacement in the

three coordinates: x,y, and z. The kinetic energy density, K, can be defined using the density ρ, and the angular velocity ω of a given vibration. The elastic potential energy, U, can be defined using the fourth-order elastic constant tensor, C, and derivatives of the displacement coordinates.[7]

$$K = \frac{1}{2}\sum_{i} \rho\omega^2 u_i^2 \qquad U = \frac{1}{2}\sum_{ijkl} C_{ijkl}\frac{\partial u_i}{\partial x_j}\frac{\partial u_k}{\partial x_l} \tag{3.2}$$

The sample we are working with is a parallelepiped and there is no known analytical solution for the displacement functions $u_i(x, y, z)$ throughout the sample for a given vibrational mode.[8] However, it is possible to approximate the displacement functions using a basis.

$$u_i = \sum_{\lambda} a_{i\lambda}\,\phi_\lambda(x, y, z) \tag{3.3}$$

$\phi_\lambda(x, y, z)$ is a basis function with index λ and coefficient $a_{i\lambda}$. If a vector $\vec{a}$ is defined to contain the coefficients for all the basis functions, it possible to write the Lagrangian in terms of matrices $\boldsymbol{E}$ and $\boldsymbol{\Gamma}$.[7]

$$L = \frac{1}{2}\omega^2 \vec{a}^T \boldsymbol{E}\vec{a} - \frac{1}{2}\vec{a}^T \boldsymbol{\Gamma}\vec{a} \tag{3.4}$$

The first term corresponds to the kinetic energy, whereas the second term corresponds to the elastic potential energy. $\boldsymbol{E}$ and $\boldsymbol{\Gamma}$ are both symmetric, and $\boldsymbol{E}$ is positive-definite. Both terms have their volume integrals incorporated into their corresponding matrices which are defined as follows. Subscripts p and q denote the elements of the matrix and they each correspond to a combination of i with λ.

$$\boldsymbol{E}_{pq} = \delta_{i_1 i_2}\int_V \rho\phi_{\lambda_1}\phi_{\lambda_2} dV \tag{3.5}$$

$$\boldsymbol{\Gamma}_{pq} = \sum_{j_1 j_2}\int_V C_{i_1 j_1 i_2 j_2}\frac{\partial\phi_{\lambda_1}}{\partial x_{j_1}}\frac{\partial\phi_{\lambda_2}}{\partial x_{j_2}} dV \tag{3.6}$$

$$p = \{i_1, \lambda_1\}, \qquad q = \{i_2, \lambda_2\} \tag{3.7}$$

By finding the stationary points of the Lagrangian, the system becomes an eigenvalue

problem where ω^2 is the generalized eigenvalue of $\boldsymbol{E}$ and $\boldsymbol{\Gamma}$.[7]

$$\boldsymbol{\Gamma}\vec{a} = \omega^2 \boldsymbol{E}\vec{a} \tag{3.8}$$

When this calculation is performed, the first 6 eigenvalues should be zero, as they correspond to the 3 translational modes and the 3 rotational modes of the sample. The vibrational modes correspond to the other eigenvalues and their resonance frequencies are $\omega/2\pi$.

In Matlab, the routine eig($\boldsymbol{\Gamma}, \boldsymbol{E}$) can be used to find ω. We have prepared versions of the direct code both in Matlab and Fortran 90. In Fortran, an option for solving the eigenvalue problem is the driver DSYGV from the LAPACK library.[9]

3.2 Basis Functions

There are many choices that exist for basis functions $\phi_\lambda(x, y, z)$ to describe the displacement $u_i(x, y, z)$. In our work, we have implemented two baseses: a power series basis, and one with linear Lagrange interpolation polynomials in the z dimension. Both of these have been used with RUS prior to our work.

3.2.1 Power Series Basis: $x^l y^m z^n$

A power series basis, $\phi_\lambda = x^l y^m z^n$, is effective because it enables the calculation of resonance frequencies for a variety of geometries, such as spheres, parallelepipeds, and cylinders.[10] Often, the power series basis has been applied with homogeneous systems. One benefit of the power series basis is elaborated on in Section 3.2.3, where this basis enables the matrices $\boldsymbol{E}$ and $\boldsymbol{\Gamma}$ to become block-diagonal with 8 blocks if the system is homogeneous.

In Fig. 3-1, we present the z components of some of these basis functions. The power series basis functions are differentiable at all points, and this is useful for a homogeneous system because the displacement field is also expected to be differentiable at all points.

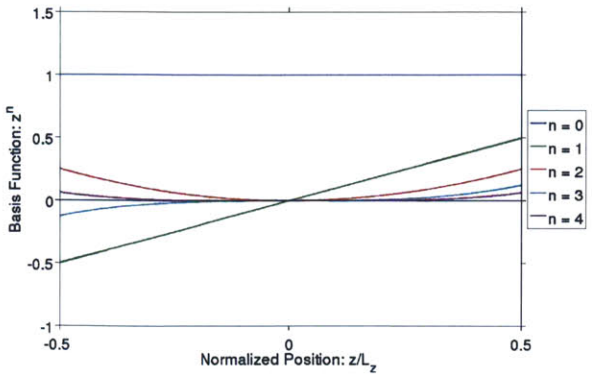

Figure 3-1: A graph of the z components of 5 power series basis functions: $x^l y^m z^n$.

Another benefit of this basis is that the expressions for its integrals are fairly simple. We use the variable I to refer to an integral in an element of either $\boldsymbol{E}$ or $\boldsymbol{\Gamma}$.

$$I_{\text{power series}} = \int_V A \left[x^{l_1} y^{m_1} z^{n_1}\right] \left[x^{l_2} y^{m_2} z^{n_2}\right] dV = \int_V A \left[x^{l_1+l_2} y^{m_1+m_2} z^{n_1+n_2}\right] dV \quad (3.9)$$

The variable A corresponds to a coefficient. In the case of $\boldsymbol{E}$, it is the density. In $\boldsymbol{\Gamma}$, it is the elastic constants multiplied by a numerical factor from the derivatives. We elaborate more on Eq. 3.9 in Sections 3.3 and 3.4.1 for the homogeneous and layered cases, respectively.

3.2.2 Interpolation Basis: $x^l y^m \Phi_n(z)$

Another basis that has been used in the literature is one with linear Lagrange interpolation polynomials in the z dimension.[11, 12, 13] Heyliger explained that the use of this basis is important because it provides a solution to one of the problems of the polynomial basis for layered materials. A layered material has different elastic constants on each side of an interface, so the displacement field has a jump discontinuity in its derivative at the interface.[11] The polynomial basis has continuous derivatives so it cannot model this property of a layered composite.

One type of function that is not differentiable at particular points is a linear piecewise function. However, in RUS, the amount of resonance frequencies obtained from the direct code is directly propertional to the number of basis functions. So

instead of viewing a linear piecewise curve as a single function, we view it as a sum of basis functions.

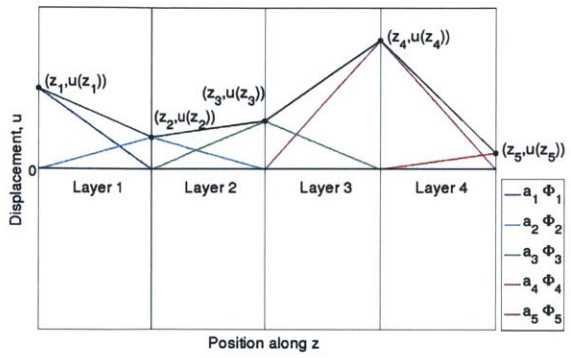

Figure 3-2: A graph of a linear piecewise function with 4 parts is presented(black). This curve is decomposed into 5 triangle functions.

A linear piecewise function with n parts (or layers) can be decomposed into $n+1$ triangle functions. These triangle functions are what is referred to in the literature as "linear Lagrange interpolation polynomials". For simplicity, I will refer to them as the "interpolation basis" in this thesis. These functions have many applications in finite-element methods. More information about them may be found in [14, 15]. Now we can discuss how the interpolation basis is constructed.

To start off, each triangle can be thought of as a piecewise function. We use the convention where the nth triangle function, $a_n\Phi_n(z)$, is peaked at the nth coordinate, (z_n, a_n). Each triangle function reaches a maximum at one of the points in the linear piecewise curve, and it reaches zero at the z values of the points next to it. If a material is characterized by L layers, then $n \in \{1, 2, ..., L, L+1\}$. Functions $\Phi_1(z)$ and $\Phi_{L+1}(z)$ correspond to the two boundaries along z. Generally, a function $\Phi_n(z)$ can be drawn using the points $(z_{n-1}, 0)$,(z_n, a_n), and $(z_{n+1}, 0)$. Fig. 3-3 presents a triangle function in the middle of the sample. We define the triangle function as a piecewise curve in Eq. 3.10.

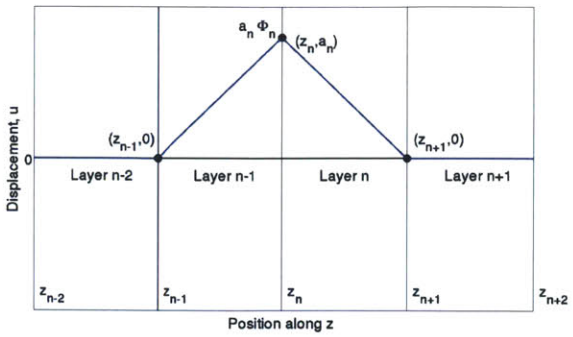

Figure 3-3: A graph of the product between a unit basis function Φ_n and its coefficient a_n is presented. The function is peaked at z_n, and it reaches zero at $z_{n\pm1}$.

$$a_n\Phi_n(z) = \begin{cases} 0 & \text{if } z \leq z_{n-1} \\ a_n\left[+\dfrac{1}{z_n - z_{n-1}}(z - z_n) + 1\right] & \text{if } z_{n-1} \leq z \leq z_n \\ a_n\left[-\dfrac{1}{z_{n+1} - z_n}(z - z_n) + 1\right] & \text{if } z_n \leq z \leq z_{n+1} \\ 0 & \text{if } z \geq z_{n+1} \end{cases} \tag{3.10}$$

Eq. 3.10 satisfies continuity at three points, and the slope is characterized by the separation between successive z_n. The unit basis functions Φ_n correspond to the terms in brackets. For calculating elements of $\mathbf{\Gamma}$, we will also need their derivatives.

$$a_n\frac{\partial\Phi_n(z)}{\partial z} = \begin{cases} 0 & \text{if } z < z_{n-1} \\ a_n\left[+\dfrac{1}{z_n - z_{n-1}}\right] & \text{if } z_{n-1} < z < z_n \\ a_n\left[-\dfrac{1}{z_{n+1} - z_n}\right] & \text{if } z_n < z < z_{n+1} \\ 0 & \text{if } z > z_{n+1} \end{cases} \tag{3.11}$$

The derivatives are undefined at the integral limits z_n, so for our calculations, we integrate inside of each layer one at a time. This basis is convenient for the part of integrating products of two basis functions, because it is not necessary to integrate throughout the entire region in z. The triangle functions are almost orthogonal to each other, because of how they reach zero at their neighboring triangles. This enables

us to charactize the integrals in the following form.

$$\int A_\ell \Phi_{n_1}(z)\Phi_{n_2}(z)dz = \begin{cases} 0 & \text{if } |n_1 - n_2| > 1 \\ \int_{z_{\min(n_1,n_2)}}^{z_{\max(n_1,n_2)}} A_\ell \Phi_{n_1}\Phi_{n_2} dz & \text{if } |n_1 - n_2| = 1 \\ \int_{z_{(n_1-1)}}^{z_{(n_1+1)}} A_\ell \left[\Phi_{n_1}\right]^2 dz & \text{if } n_1 = n_2 \end{cases} \tag{3.12}$$

A_ℓ corresponds to a property of layer ℓ, and it is not related to the value of a_n. The layer index takes values $\ell \in \{1, 2, ..., L\}$. In $\boldsymbol{E}$, the value of A_ℓ corresponds to the density ρ_ℓ. In $\boldsymbol{\Gamma}$, the value of A_ℓ corresponds to an elastic constant, such as $[C_{11}]_\ell$. When $n_1 = n_2$ and $n_1 \in \{2, 3, ..., L-1, L\}$, the integral should be separated into two parts, as A_ℓ could have different values inside of each layer. The integral limits in Eq. 3.12 can also be used if the basis functions have derivatives applied to them.

The interpolation basis can be used for both homogeneous systems and layered systems. In ARB samples, as the interface area-to-volume ratio increases, it is expected that the composite approaches a configuration with constant layer widths, $z_n - z_{n-1} = d$. In our calculations, we use this approximation. This motivated us to calculate analytical solutions for the integrals, and we present them in Table 3.1. The integrals near the boundaries, where n_1 and n_2 are both equal to either 1 or $L+1$, can be derived from case 4 using the substitution of $A_0 = A_{L+1} = 0$. These analytical solutions are helpful because they greatly speed up the time required for the computations of the matrix elements.

Table 3.1: Analytical solutions to z integrals of interpolation basis. The composite is assumed to have constant layer width d and equal volume fractions, $\nu_{\text{Cu}} = \nu_{\text{Nb}} = 0.5$.

Case	1	2	3	4
Relation	$\lvert n_1 - n_2\rvert > 1$	$n_1 = n_2 + 1$	$n_1 = n_2 - 1$	$n_1 = n_2$
$\int A_\ell \Phi_{n_1}\Phi_{n_2} dz$	0	$\frac{d}{6}A_{\min(n_1,n_2)}$	$\frac{d}{6}A_{\min(n_1,n_2)}$	$\frac{d}{3}(A_{n_1-1} + A_{n_1})$
$\int A_\ell \frac{\partial\Phi_{n_1}}{\partial z}\Phi_{n_2} dz$	0	$\frac{1}{2}A_{\min(n_1,n_2)}$	$\frac{-1}{2}A_{\min(n_1,n_2)}$	$\frac{1}{2}(A_{n_1-1} - A_{n_1})$
$\int A_\ell \Phi_{n_1}\frac{\partial\Phi_{n_2}}{\partial z} dz$	0	$\frac{-1}{2}A_{\min(n_1,n_2)}$	$\frac{1}{2}A_{\min(n_1,n_2)}$	$\frac{1}{2}(A_{n_1-1} - A_{n_1})$
$\int A_\ell \frac{\partial\Phi_{n_1}}{\partial z}\frac{\partial\Phi_{n_2}}{\partial z} dz$	0	$\frac{-1}{d}A_{\min(n_1,n_2)}$	$\frac{-1}{d}A_{\min(n_1,n_2)}$	$\frac{1}{d}(A_{n_1-1} + A_{n_1})$

3.2.3 General Properties

Truncation of Baseses

The accuracy of the calculated resonance frequencies increases with the number of basis functions. It is not possible for us to work with an infinite basis, so we must truncate the basis. There are two common conventions used for truncating the power series basis $x^l y^m z^n$. To define these conventions, we consider how each basis function is represented by three integer values: l, m, and n.

One convention that was used by Visscher was to limit the exponents with a constant upper bound, $0 \leq l, m, n \leq M$, where M is an integer.[10] This causes the highest polynomials to have the same exponent in each dimension, $x^M y^M z^M$. With this convention, the order R of the matrices is $R = 3(M+1)^3$.

Another convention is one that is used in the program rpr.exe from Migliori, where the sum of the exponents is limited by an upper bound, $0 \leq l+m+n \leq N$, where N is also an integer.[16] This causes the highest polynomials to depend on only one of the three coordinates, either x^N, y^N, or z^N. In this case, $R = \frac{1}{2}(N+1)(N+2)(N+3)$.

When we use the interpolation basis $x^l y^m \Phi_n(z)$, we use a different truncation for the z dimension, $1 \leq n \leq L+1$, where L is the number of total layers. As for the xy functions, a trunctation of either N or M can be used with the interpolation basis.

In Table 3.2, we present the 4 four combinations of basis functions with truncations and their values of R. The coefficient of 3 in every R comes from how there are three displacement coordinates, $i \in \{1,2,3\} = \{x, y, z\}$. Each of these 4 combinations can be applied to either a homogeneous system or a layered system, according to the preference of the user.

Table 3.2: The value of R is presented for different basis functions and truncations.

Basis Functions	Truncations		R
$x^l y^m z^n$	$0 \leq l+m+n \leq N$		$3(N+1)(N+2)(N+3)/3!$
$x^l y^m z^n$	$0 \leq l, m, n \leq M$		$3(M+1)^3$
$x^l y^m \Phi_n(z)$	$0 \leq l+m \leq N$	$1 \leq n \leq L+1$	$3\left[(N+1)(N+2)/2!\right](L+1)$
$x^l y^m \Phi_n(z)$	$0 \leq l, m \leq M$	$1 \leq n \leq L+1$	$3\left[(M+1)^2\right](L+1)$

The values of L, M, and N are chosen by the user of the direct code. Increasing these parameters generally increases the accuracy, at the cost of computation time. However, there are cases where a large value of these parameters can generate numerical problems with truncations, as the matrix $\boldsymbol{E}$ could lose its property of being positive definite.[7] We also encountered this problem in our fortran codes and it was noticable because the eigenvalue routine began outputting negative resonance frequencies which do not have a physical meaning. We found that changing the precision of the code from single to double, allowed the code to take larger values of L, M, and N while outputing valid eigenvalues. In her Master's Thesis, María Teresa Cerda Guevara explains that the program rpr.exe could exhibit problems of numerical truncation at about $N = 20$.[17] Based on this, we performed most of our simulations below $N = 20$.

Grouping of Basis Functions

For our calculations, we define the origin to be at the center of the material. Using the symmetries of the system, it is possible to simplify the calculations of the integrals. Heyliger explained using the values of i, l, and m that it is possible to organize the basis functions into 4 groups that are orthogonal with each other.[11]

Table 3.3: The 4 groups of basis functions corresponding to symmetry in the xy plane are presented. E denotes an even exponent, while O denotes an odd exponent. This table was adapted from Heyliger et al.[11]

Group	i	x^l	y^m	Example
1	1	E	E	$u_1 = x^2y^2$
	2	O	O	$u_2 = xy$
	3	O	E	$u_3 = xy^2$
2	1	E	O	$u_1 = x^2y$
	2	O	E	$u_2 = xy^2$
	3	O	O	$u_3 = xy$
3	1	O	O	$u_1 = xy$
	2	E	E	$u_2 = x^2y^2$
	3	E	O	$u_3 = x^2y$
4	1	O	E	$u_1 = xy^2$
	2	E	O	$u_2 = x^2y$
	3	E	E	$u_3 = x^2y^2$

The groups in Table 3.3 can be used if the samples (or the constituents in the layered case) have at least orthotropic symmetry. We can examine the effect of using these groups with an example. Suppose we were to construct a power series basis using a truncation of $N = 1$. There are a total of 12 possible basis functions. We can organize them according to their group numbers as shown in Table 3.4.

Table 3.4: The 12 power series basis functions of $N = 1$ were ordered by group.

Index	i	l	m	n	Group	$\phi_{i,\lambda}(x,y,z)$
1	1	0	0	0	1	$u_1 = 1$
2	1	0	0	1	1	$u_1 = z$
3	3	1	0	0	1	$u_3 = x$
4	1	0	1	0	2	$u_1 = y$
5	2	1	0	0	2	$u_2 = x$
6	2	0	0	0	3	$u_2 = 1$
7	2	0	0	1	3	$u_2 = z$
8	3	0	1	0	3	$u_3 = y$
9	1	1	0	0	4	$u_1 = x$
10	2	0	1	0	4	$u_2 = y$
11	3	0	0	0	4	$u_3 = 1$
12	3	0	0	1	4	$u_3 = z$

In Eq. 3.6, when we compute the matrix elements of $\boldsymbol{\Gamma}$, the numbers j_1 and j_2 vary from 1 to 3, so there are a total of nine terms. When we compute matrix elements of $\boldsymbol{E}$, there is only one term. In either case, when an integral contains basis functions from different groups, the matrix element is zero based on one of the following reasons:

- the product of the two basis functions is odd
- the basis functions have different displacement coordinates i (in the case of $\boldsymbol{E}$)
- the coefficient $C_{i_1 j_1 i_2 j_2}$ is zero (in the case of $\boldsymbol{\Gamma}$).

The use of these groups causes the matrices of $\boldsymbol{E}$ and $\boldsymbol{\Gamma}$ to become block-diagonal.

$$\begin{bmatrix} \boldsymbol{\Gamma_1} & 0 & 0 & 0 \\ 0 & \boldsymbol{\Gamma_2} & 0 & 0 \\ 0 & 0 & \boldsymbol{\Gamma_3} & 0 \\ 0 & 0 & 0 & \boldsymbol{\Gamma_4} \end{bmatrix} \vec{a} = \omega^2 \begin{bmatrix} \boldsymbol{E_1} & 0 & 0 & 0 \\ 0 & \boldsymbol{E_2} & 0 & 0 \\ 0 & 0 & \boldsymbol{E_3} & 0 \\ 0 & 0 & 0 & \boldsymbol{E_4} \end{bmatrix} \vec{a} \tag{3.13}$$

The number of blocks is equivalent to the number of groups, which is 4 in this case. The resonance frequencies of a block in Eq. 3.13 can be calculated independently

from those of the other blocks. This speeds up the calculations because it is easier to calculate the eigenvalues of 4 small matrices than 1 large matrix. Also, this enables us to initialize the majority of the values in the matrices to zero. In each block, only about one-half of the elements need to calculated, because the matrices are symmetric.

Ohno explained that if a polynomial basis is used with a homogeneous material, the basis functions can be organized into 8 orthogonal groups.[18] This accelerates the calculations further than in the case of 4 groups. Ohno implemented these 8 groups with Legendre polynomials, but they are also often used with the power series basis.

Table 3.5: The 8 groups of basis functions corresponding to symmetry in 3 dimensions are presented. i is the displacement coordinate. E denotes an even exponent, while O denotes an odd exponent. This table was adapted from Ohno et al.[18]

Group	i	x^l	y^m	z^n	Example
1	1	O	E	E	$u_1 = xy^2z^2$
	2	E	O	E	$u_2 = x^2yz^2$
	3	E	E	O	$u_3 = x^2y^2z$
2	1	E	E	E	$u_1 = x^2y^2z^2$
	2	O	O	E	$u_2 = xyz^2$
	3	O	E	O	$u_3 = xy^2z$
3	1	O	O	E	$u_1 = xyz^2$
	2	E	E	E	$u_2 = x^2y^2z^2$
	3	E	O	O	$u_3 = x^2yz$
4	1	O	E	O	$u_1 = xy^2z$
	2	E	O	O	$u_2 = x^2yz$
	3	E	E	E	$u_3 = x^2y^2z^2$
5	1	O	O	O	$u_1 = xyz$
	2	E	E	O	$u_2 = x^2y^2z$
	3	E	O	E	$u_3 = x^2yz^2$
6	1	E	E	O	$u_1 = x^2y^2z$
	2	O	O	O	$u_2 = xyz$
	3	O	E	E	$u_3 = xy^2z^2$
7	1	E	O	E	$u_1 = x^2yz^2$
	2	O	E	E	$u_2 = xy^2z^2$
	3	O	O	O	$u_3 = xyz$
8	1	E	O	O	$u_1 = x^2yz$
	2	O	E	O	$u_2 = xy^2z$
	3	O	O	E	$u_3 = xyz^2$

3.3 Homogeneous Systems

Integrals

A homogeneous system has a uniform density and elastic constants matrix throughout the sample, so its calculations are simpler than those of a layered system. A homogeneous sample can be modeled with either the power series basis or the interpolation basis, but here the power series basis is generally preferred as it is differentiable at all points and that is consistent with the displacement field. In both cases, the integrals in $\boldsymbol{E}$ and $\boldsymbol{\Gamma}$ become simplified. We refer to these integrals as I.

We use a subscript s to denote the sum of two integers. For example, $l_s = l_1 + l_2$, and similarly for m_s and n_s. We use L_r to denote the length of the r-th dimension of the sample. In the power series basis, the integrals become:

$$I^{\text{homogeneous}}_{\text{power series}} = \begin{cases} \dfrac{8A\left[L_1^{(l_s+1)} L_2^{(m_s+1)} L_3^{(n_s+1)}\right]}{[l_s+1]\,[m_s+1]\,[n_s+1]} & \text{if } \{l_s, m_s, n_s\} \text{ are even} \\ 0 & \text{otherwise} \end{cases} \tag{3.14}$$

The expressions in Eq. 3.14 are exact for the case of $\boldsymbol{E}$. These expressions can be used in $\boldsymbol{\Gamma}$ only after the derivatives are accounted for. A takes the value of the density ρ in $\boldsymbol{E}$, or an elastic constant $C_{i_1 j_1 i_2 j_2}$ in $\boldsymbol{\Gamma}$.

If we use the interpolation basis with a homogeneous system, we can use a similar expression for the integrals:

$$I^{\text{homogeneous}}_{\text{interpolation}} = \begin{cases} \dfrac{4\left[L_1^{(l_s+1)} L_2^{(m_s+1)}\right]}{[l_s+1]\,[m_s+1]} I_Z & \text{if } \{l_s, m_s\} \text{ are even} \\ 0 & \text{otherwise} \end{cases} \tag{3.15}$$

This is essentially the xy component of Eq. 3.14 times I_Z, where I_Z is an integral that can be selected from Table 3.1. This is quicker for homogeneous systems than for layered systems, because the terms A_ℓ become constants in the homogeneous case.

Simulations: Homogeneous Olivine System

We now conduct simulations with a homogeneous system to study the properties of the interpolation basis. We choose a system that was studied by both Heyliger[11] and Ohno[18]. The material is called olivine, and it has orthotropic symmetry. Its dimensions are $2.745 \times 2.832 \times 2.015\text{mm}^3$ and its density is $3.316\ \text{g/cm}^3$. The elastic constants in units of $(10^{12}\text{dynes/cm}^2)$ are $C_{11} = 3.24$, $C_{22} = 1.96$, $C_{33} = 2.32$, $C_{12} = 0.715$, $C_{13} = 0.715$, $C_{23} = 0.688$, $C_{44} = 0.639$, $C_{55} = 0.779$, and $C_{66} = 0.788$.

Table 3.6: Resonance frequencies of a homogeneous sample of olivine using the interpolation basis and the power series basis. $M = 7$ was used as a truncation. For the interpolation, we used $L = 16$. Frequencies are presented in units of MHz.

Mode	Interpolation $x^l y^m \Phi_n(z)$	Power Series $x^l y^m z^n$	Mode	Interpolation $x^l y^m \Phi_n(z)$	Power Series $x^l y^m z^n$
1	0.69350	0.69299	26	1.8554	1.8505
2	0.93039	0.92988	27	1.8921	1.8872
3	1.0306	1.0290	28	1.8981	1.8903
4	1.0392	1.0391	29	1.8994	1.8957
5	1.0895	1.0895	30	1.9313	1.9264
6	1.1604	1.1584	31	1.9529	1.9492
7	1.2097	1.2096	32	1.9791	1.9732
8	1.2260	1.2248	33	2.0704	2.0672
9	1.2324	1.2311	34	2.0752	2.0696
10	1.3114	1.3112	35	2.1506	2.1470
11	1.3189	1.3166	36	2.1554	2.1522
12	1.4124	1.4117	37	2.1796	2.1747
13	1.4145	1.4129	38	2.2392	2.2318
14	1.5423	1.5401	39	2.2530	2.2472
15	1.6374	1.6359	40	2.2706	2.2684
16	1.6546	1.6479	41	2.2780	2.2704
17	1.6569	1.6547	42	2.2782	2.2750
18	1.6821	1.6805	43	2.2859	2.2777
19	1.6859	1.6812	44	2.3383	2.3281
20	1.6867	1.6820	45	2.3626	2.3544
21	1.7487	1.7443	46	2.3801	2.3730
22	1.7604	1.7588	47	2.3996	2.3962
23	1.7824	1.7781	48	2.4047	2.4027
24	1.8068	1.8030	49	2.4284	2.4246
25	1.8262	1.8246	50	2.4630	2.4561

We calculated the resonance frequencies using the power series basis and the interpolation basis. We present our results from this simulation in Table 3.6. It may also be possible to compare our results with those of both Heyliger and Ohno.[11] There is moderate agreement between our calculations and theirs. However, we used a power series in the xy plane whereas they both used Legendre polynomials. This

could explain differences between our calculations.

Qualitatively, there appears to be good agreement between the power series basis and the interpolation basis. For the interpolation basis in Table 3.6, we divided the homogenous sample into 16 layers. However, Table 3.6 alone does not provide us with information about the interpolation basis at different layer widths. This motivated us to conduct a simulation where we vary L, the number of layers in the interpolation basis, and calculate the resonance frequencies while keeping the geometry unchanged. We then calculated the residual sum of squares (RSS) at different values of L relative to the resonance frequencies from the power series basis. We present these simulation results in Fig. 3-4.

These simulations were conducted at different values of M and comparing different amounts of resonances frequencies. In RUS, often at least 45 modes are used to fit for the 9 elastic constants of an orthotropic sample [5], but we extended our simulations up to the first 135 modes. The values of RSS were normalized by the square of the number of frequencies compared, in order to have the curves nearly line up.

From Fig. 3-4a, these simulations appear to show that as the number of total layers increases, the RSS approaches 0. However, Fig. 3-4b is on a logarithmic scale and it shows that the curves are not entirely monotonic. The curves with $M = 5$ and $M = 6$ exhibit a decrease that appears to be exponential, they reach a minimum value, and then they increase. At a given value of M, as the number of modes decreases from 135 to 90 to 45, the magnitude of the RSS decreases and the minimum occurs at a larger L. Similarly, as the value of M increases, the minimum also occurs at higher value of L. For instance, the minimum is not visible at $M = 7$ when we consider up to 53 layers with 135 modes or less.

These features suggest that if it were possible to increase M or N endlessly, then the minimum would continue moving to higher L, the curve would continue decreasing, and the RSS would converge to 0. As the value of L would increase, the resonance frequencies from a homogeneous sample with the interpolation basis would converge to those of a homogeneous sample with the power series basis. We use this point in Section 3.4.3.

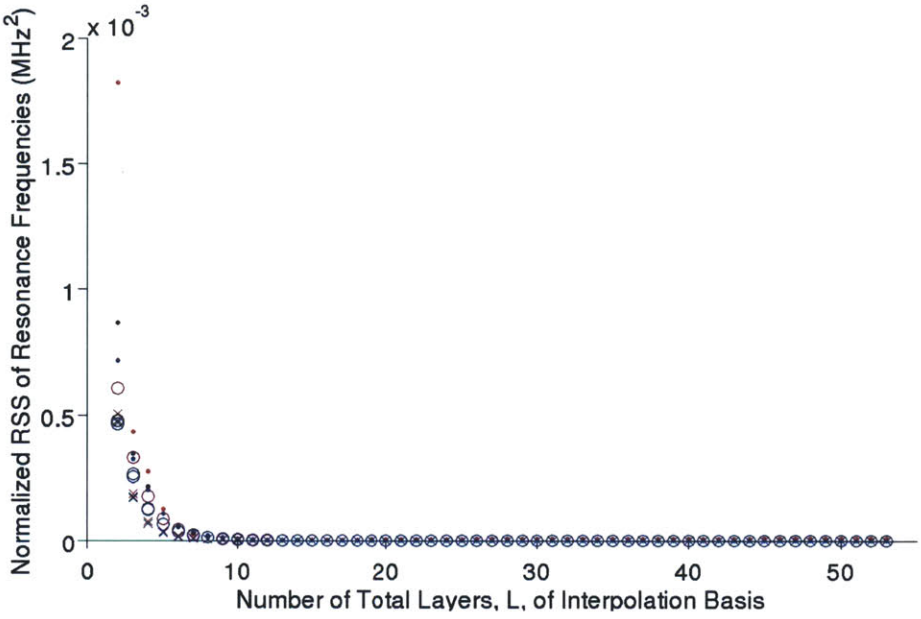

(a) Normalized RSS as a function of L.

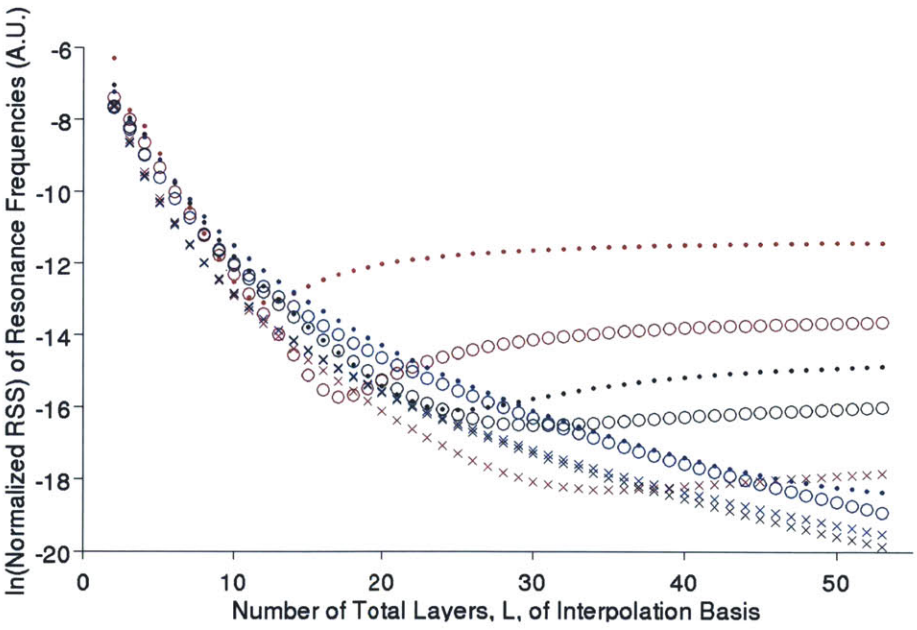

(b) Logarithmic Graph as a function of L.

Figure 3-4: A simulation with olivine was conducted. RSS was calculated between the resonance frequencies from the power series basis and the interpolation basis. Truncations of $M = 5$ (red), $M = 6$ (black), and $M = 7$(blue) were used. RSS was computed using 45 modes (X), 90 modes(O), and 135 modes($\cdot$).

3.4 Layered Systems

3.4.1 Differences from Homogeneous Systems

It is possible to run a layered code using the power series basis or the interpolation basis. However, it is generally not recommended to run the layered code with the power series basis because it cannot represent the discontinuities in the slope of the displacement field as Heyliger explained.[11] Regardless of which basis is used, changes are made to how the integrals are computed.

$$I^{\text{layered}} = \left[\int_{\text{area}} f(x,y)\,dxdy\right]\left[\int_{\text{height}} A\,g(z)dz\right] \tag{3.16}$$

The main idea is that we separate the integral into two parts. If the material is layered, then A is not constant throughout the z dimension, but it depends on each layer. We define the layer index to be ℓ, and we take the total number of layers to be L. It is possible to integrate each layer in z separately with their respectively coefficients A_ℓ.

$$I = \left[\int_{\text{area}} f(x,y)\,dxdy\right]\left[\sum_{\ell=1}^{L}\int_{\Delta z_\ell} A_\ell\,g(z)dz\right] \tag{3.17}$$

We can reduce this expression for the two baseses we are considering. In the case of the layered code with the interpolation basis, it is the same as with Eq. 3.15, but A_ℓ is not constant.

$$I^{\text{layered}}_{\text{power series}} = \begin{cases} \left[\dfrac{4\left[L_1^{(l_s+1)}L_2^{(m_s+1)}\right]}{[l_s+1]\,[m_s+1]}\right]\left[\displaystyle\sum_{\ell=1}^{L}\int_{\Delta z_\ell} A_\ell\,z^{n_1+n_2}dz\right] & \text{if } \{l_s,m_s\} \text{ are even} \\ 0 & \text{otherwise} \end{cases} \tag{3.18}$$

$$I^{\text{layered}}_{\text{interpolation}} = \begin{cases} \dfrac{4\left[L_1^{(l_s+1)}L_2^{(m_s+1)}\right]}{[l_s+1]\,[m_s+1]} I_Z & \text{if } \{l_s,m_s\} \text{ are even} \\ 0 & \text{otherwise} \end{cases} \tag{3.19}$$

Both of these expressions for I^{layered} are directly applicable for $\boldsymbol{E}$. However, they can be applied for $\boldsymbol{\Gamma}$ only after derivatives can been accounted for.

3.4.2 Simulations

System: "Layered Sandwich"

We now conduct simulations with a layered system to study the convergence behavior of both baseses. We choose a hypothetical system that was studied by both Heyliger[11] and Visscher[10]. Visscher referred to it as the "Layered Sandwich".

The sample is composed of two blocks, each containing isotropic symmetry. Its dimensions are 0.4 x 0.6 x 0.8 cm^3. Material 1 has a density of 2 g/cm^3, and it has isotropic symmetry with $C_{11} = 1.2$ and $C_{44} = 0.4$ dynes/cm^2. Material 2 has a density of 10 g/cm^3, and it has isotropic symmetry with $C_{11} = 6.0$ and $C_{44} = 2.0$ dynes/cm^2. The interface between the two materials is along the middle of the sample, which is where we define the $z = 0$ plane to be. We present a picture of the sample in Fig. 3-5a.

Table 3.7: Resonance frequencies of the "layered sandwich" were calculated using the interpolation basis and the power series basis. $M = 7$ was used as a truncation. For the interpolation, we used $L = 16$. Frequencies are presented in units of MHz.

Mode	Interpolation $x^l y^m \Phi_n(z)$	Power Series $x^l y^m z^n$	Mode	Interpolation $x^l y^m \Phi_n(z)$	Power Series $x^l y^m z^n$
1	0.23607	0.24570	26	0.77072	0.77172
2	0.25136	0.26285	27	0.77546	0.78531
3	0.27849	0.29159	28	0.78031	0.78560
4	0.39916	0.40371	29	0.79411	0.79058
5	0.43077	0.43714	30	0.79719	0.79681
6	0.43640	0.44334	31	0.79884	0.80148
7	0.45190	0.47064	32	0.82054	0.82265
8	0.47744	0.48496	33	0.83217	0.83571
9	0.48136	0.49386	34	0.83592	0.84178
10	0.51366	0.51973	35	0.85864	0.85245
11	0.52649	0.54426	36	0.85867	0.85673
12	0.54065	0.54518	37	0.86369	0.86721
13	0.57475	0.57444	38	0.87598	0.87379
14	0.58467	0.58684	39	0.87904	0.88121
15	0.59146	0.59244	40	0.88335	0.88168
16	0.60809	0.60857	41	0.88753	0.88796
17	0.65150	0.65569	42	0.88910	0.89323
18	0.66413	0.66160	43	0.90602	0.90896
19	0.67148	0.68307	44	0.91079	0.91903
20	0.70332	0.70293	45	0.91978	0.92136
21	0.70986	0.70561	46	0.92587	0.92367
22	0.71588	0.71765	47	0.93917	0.94036
23	0.73721	0.72869	48	0.94242	0.94723
24	0.75128	0.75305	49	0.94482	0.95313
25	0.75887	0.76037	50	0.94566	0.95896

Initially, we calculated the resonance frequencies of this two-block system using the power series basis and the interpolation basis. We present our results of this simulation in Table 3.7. It is possible to compare our calculations with the results that were published by Heyliger.[11]

In our simulation, we obtained good agreement with the values from Heyliger's code for the basis that uses linear Lagrange interpolation polynomials. Although we did not find strong agreement with the values from the Visscher code, our simulation seems to qualitatively illustrate the property explained by Heyliger, that the use of differentiable functions in the z dimension generally makes the system stiffer and causes higher resonance frequencies. In 38 out of the 50 frequencies we calculated, this was evidenced as the code with the linear Lagrange interpolation polynomials produced lower frequencies. This corresponds to 76% of the frequencies we considered with this two-layer system.

Average and Effective Elastic Constants

We are interested in studying the convergence behavior of the layered code, both in the case of the power series basis and in the case of the interpolation basis. Our goal here is to represent the layered code with large interface area-to-volume ratio, by a homogeneous code. For this, we need to decide on an elastic constants matrix that can represent the composite. To start off, we list the elastic constants matrix of the two materials.

$$C^1 = \begin{bmatrix} 1.2 & 0.4 & 0.4 & 0 & 0 & 0 \\ 0.4 & 1.2 & 0.4 & 0 & 0 & 0 \\ 0.4 & 0.4 & 1.2 & 0 & 0 & 0 \\ 0 & 0 & 0 & 0.4 & 0 & 0 \\ 0 & 0 & 0 & 0 & 0.4 & 0 \\ 0 & 0 & 0 & 0 & 0 & 0.4 \end{bmatrix} \qquad C^2 = \begin{bmatrix} 6 & 2 & 2 & 0 & 0 & 0 \\ 2 & 6 & 2 & 0 & 0 & 0 \\ 2 & 2 & 6 & 0 & 0 & 0 \\ 0 & 0 & 0 & 2 & 0 & 0 \\ 0 & 0 & 0 & 0 & 2 & 0 \\ 0 & 0 & 0 & 0 & 0 & 2 \end{bmatrix} \tag{3.20}$$

According to Grimsditch, a layered parallelepiped that is composed of two materials can be characterized by a set of "effective elastic constants" which we label C^{eff}.[19] Grimsditch provides the equations for these parameters using composite theory, and

we use them to calculate C^{eff} for the layered sandwich. We also calculate C^{ave} which we refer to as the arithmetic mean between the elastic constants matrices of the two materials.

$$C^{\text{ave}} = \begin{bmatrix} 3.6 & 1.2 & 1.2 & 0 & 0 & 0 \\ 1.2 & 3.6 & 1.2 & 0 & 0 & 0 \\ 1.2 & 1.2 & 3.6 & 0 & 0 & 0 \\ 0 & 0 & 0 & 1.2 & 0 & 0 \\ 0 & 0 & 0 & 0 & 1.2 & 0 \\ 0 & 0 & 0 & 0 & 0 & 1.2 \end{bmatrix} \tag{3.21}$$

$$C^{\text{eff}} = \begin{bmatrix} 3.42 & 1.02 & 0.67 & 0 & 0 & 0 \\ 1.02 & 3.42 & 0.67 & 0 & 0 & 0 \\ 0.67 & 0.67 & 2 & 0 & 0 & 0 \\ 0 & 0 & 0 & 0.67 & 0 & 0 \\ 0 & 0 & 0 & 0 & 0.67 & 0 \\ 0 & 0 & 0 & 0 & 0 & 1.2 \end{bmatrix} \tag{3.22}$$

In our simulations, we compare the layered codes with a homogeneous code that uses C^{ave} and one that uses C^{eff}.

Changing the Configuration

We now conduct a series of simulations of the resonance frequencies of the two-block system. From a numerical standpoint, this is going to be similar to the olivine simulations because we vary L, the number of layers in the interpolation basis. However, here we change the configuration of the system from one simulation to the next.

We start with the standard 2-block system that was studied by Heyliger and Visscher.[10, 11] We calculate the resonance frequencies of the layered system using the layered code. We then consider a homogeneous block of the same dimensions with the average elastic constants C^{ave} and calculate its resonance frequencies. We calculate the sum of squared residuals (SSR) between the layered code and the homogeneous code with C^{ave}. Next we consider another homogeneous block, but this one has the effective elastic constants C^{eff} and calculate its resonance frequencies. Finally we calculate the SSR between the layered code and the homogeneous code with C^{eff}.

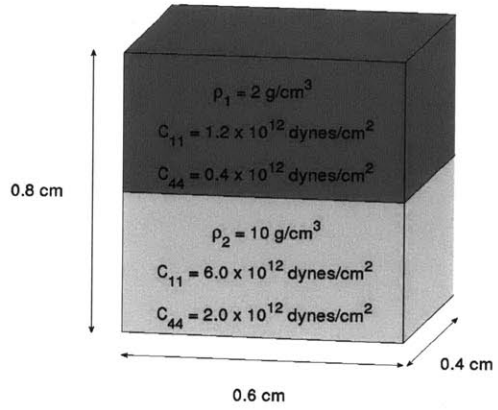

(a) Parameters of the sublayers.

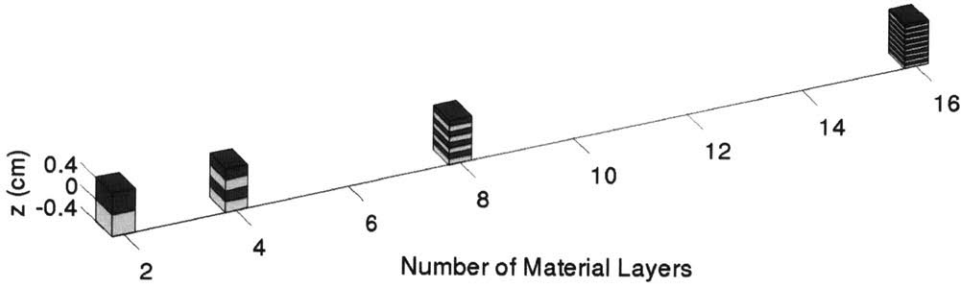

(b) The number of material layers were increased successively by factors of 2.

Figure 3-5: A simulation with the "Layered Sandwich" was conducted.

Next, we replace the 2-block system by a 4-block system and repeat our calculations. In the case of the power series basis, we ran our simulations up to 64 material layers. In the case of the interpolation basis, we ran our simulations up to 32 material layers. We illustrate the first 4 systems of these simulations in Fig. 3-5b.

Convergence Behavior of Power Series Basis

We first conduct our simulations using the power series basis, $x^l y^m z^n$. We vary the number of material layers from 2 to 64. For each case, we use $M = 7$ to truncate the basis. We calculate the resonance frequencies for the layered system and two homogeneous systems and we determine the SSR between the first 50 resonance frequencies. We present our results in Fig. 3-6.

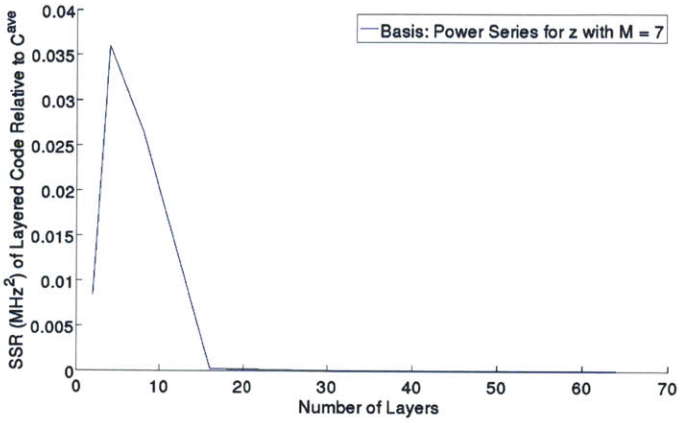

(a) Convergence of $x^l y^m z^n$ to C^{ave}

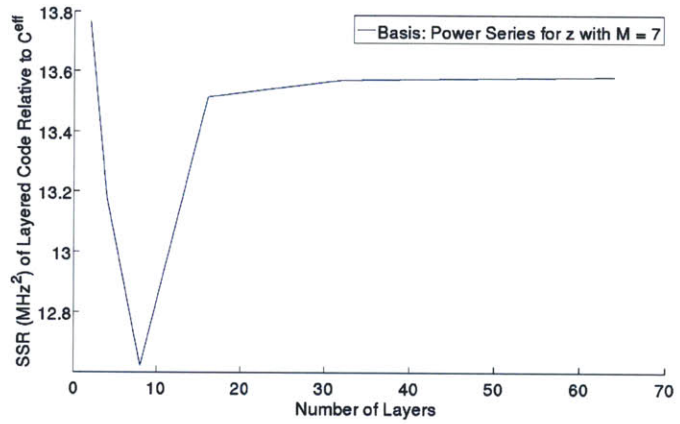

(b) Divergence of $x^l y^m z^n$ from C^{eff}.

Figure 3-6: A simulation of the "Layered Sandwich" was conducted using the power series basis. SSR was calculated between the resonance frequencies from the layered code and a homogeneous code. The homogeneous code used either average elastic constants (top) or effective elastic constants (bottom).

In Fig. 3-6a, the SSR converges to zero. Thus, the resonance frequencies of a layered system with the power series basis approach those of a homogeneous system with "average elastic constants" C^{ave}. In Fig. 3-6b, the SSR approaches a finite nonzero value. Thus, the resonance frequencies of a layered system with the power series basis diverge from those of a homogeneous system with "effective elastic constants" C^{eff}. This contradicts the analytical results from composite theory. There is strange behavior below 8 layers, but the long-term convergence seems unaffected by this.

Convergence Behavior of Interpolation Basis

Next, we conduct our simulations using the interpolation basis, $x^l y^m \Phi_n(z)$. We vary the number of material layers from 2 to 32. For each case, we use $M = 7$ to truncate the xy functions. We subdivided each material layer in order to keep the total number of layers, L, at a constant value of 64. We calculated the resonance frequencies for the layered system and two homogeneous systems and we determine the SSR between the first 50 resonance frequencies. We present our results in Fig. 3-7.

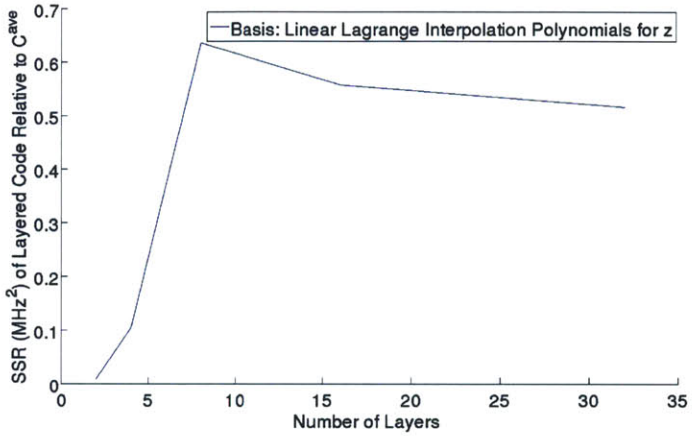

(a) Divergence of $x^l y^m \Phi_n(z)$ from C^{ave}

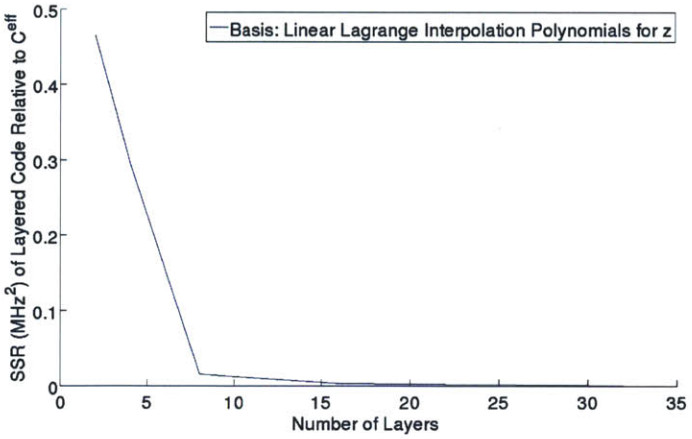

(b) Convergence of $x^l y^m \Phi_n(z)$ to C^{eff}

Figure 3-7: A simulation of the "Layered Sandwich" was conducted using the interpolation basis. SSR was calculated between the resonance frequencies from the layered code and the homogeneous code. The homogeneous code used either average elastic constants (top) or effective elastic constants (bottom). L had a constant value of 64.

In Fig. 3-7a, we find that the SSR approaches a nonzero value. This means that the resonance frequencies of a layered system with the power series basis diverge from those of a homogeneous system with "average elastic constants" C^{ave}. In Fig. 3-7b, we find that the SSR converges to zero. This means that the resonance frequencies of a layered system with the interpolation basis approach those of a homogeneous system with "effective elastic constants" C^{eff}.

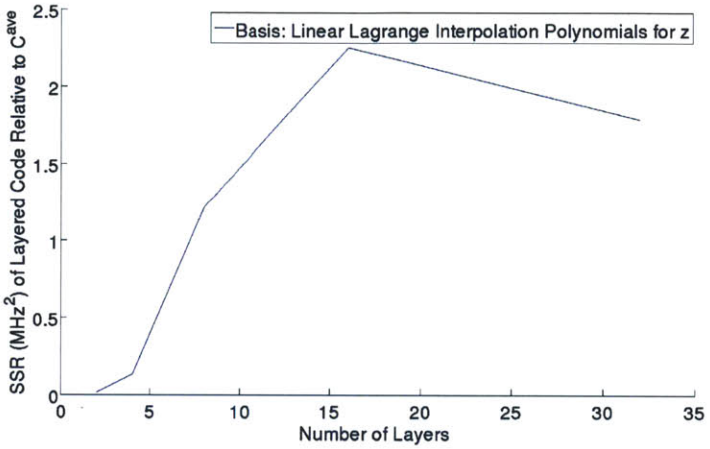

(a) Divergence of $x^l y^m \Phi_n(z)$ from C^{ave}

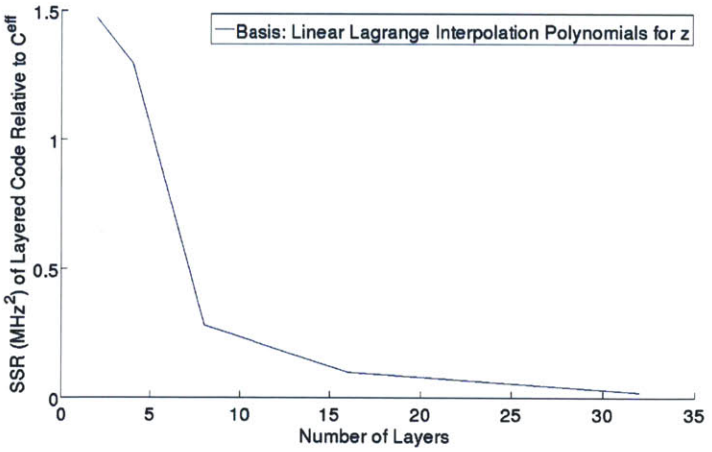

(b) Convergence of $x^l y^m \Phi_n(z)$ to C^{eff}

Figure 3-8: A simulation of the "Layered Sandwich" was conducted using the interpolation basis. SSR was calculated between the resonance frequencies from the layered code and the homogeneous code. The homogeneous code used either average elastic constants (top) or effective elastic constants (bottom). L had a value of 8 times the number of material layers in each case. $M = 1$ was used for the xy functions.

We also conducted simulations where we kept the value of L variable and we kept the number of sublayers inside each material layer at a constant value of 8. We present these simulations in Fig. 3-8. Here $M = 1$ was used for the xy functions. Although a value of $M = 1$ is less accurate, we find that the qualitative features of the graph are the same as those of the previous case. The reason we used a much smaller value of M was because the computer was not capable of completing this simulation at large values of M.

We have found that whether the number of subdivisions in a material layer is held constant or number of total layers L is held constant, the interpolation basis exhibits convergence to a system with "effective elastic constants" as the number of material layers increases.

3.4.3 Applications for Composite Systems

To the best of our knowledge, there weren't simulations that exhibited the properties of the baseses with increasing interface area-to-volume ratio, or an increasing number of material layers. Our simulations have contributed information about the interpolation basis both for layered and homogeneous systems.

We have 3 ARB Cu/Nb samples that we are studying. The first sample has 12 layers, while each of the other 2 have over 8000 layers. It is not realistic to run the layered interpolation code around 8000 layers, as it would require too much time to just compute the matrix elements. Not only that, but if we would want to use a value of $M = 7$ or higher for the truncation of the xy functions, this would require over $R = 1.5\text{x}10^6$ basis functions. This would require matrices with over 10^{12} elements. The current eigenvalue routines we have are not capable of solving such systems. Normally, this would be a problem, but our simulations provide a solution for this.

From Fig. 3-7 and 3-8, we find that instead of using the layered interpolation code for a composite with large interface area-to-volume ratio, we can use a homogeneous interpolation code to model the composite and any values of elastic constants would correspond to the effective values C^{eff} of the composite. Then, from Fig. 3-4, we find that a homogeneous interpolation code with low layer widths can be replaced by a

homogeneous power series code with the same parameters. This means that instead of using a code with 8000 layers, we can homogenize the system and use the power series basis to fit for the effective elastic constants. This serves as our motivation for using the homogeneous code with samples 2 and 3 which have a large interface area-to-volume ratio.

Simulation of Sample 1

For sample 1, we had to decide whether we would use the layered code or the homogeneous code. The homogeneous code is quicker, so we performed another simulation to assess the validity of its use. In this simulation, we considered sample 1 in two forms. One form was as a composite with isotropic layers of copper and niobium. The other form was as a homogeneous system. In both cases the geometry is the same. We will now discuss the input parameters used in each case.

For the layered case, we used the isotropic elastic constants from the Table 6.1. For sample 1, we measured the density to be about 8.685 g/cm^3. The density of copper is 8.932 and that of niobium is 8.578.[20] If we were to assume the composite were 50% Cu and 50% Nb by volume, then we would expect the density of the sample to be about 8.755. Our measured density is lower, and one explanation for this would be a void percentage of about 0.79%. In order to perform our simulation with the layered Cu/Nb system, we decrease the densities of copper and niobium each by this void percentage, so that $\rho_{Cu} \approx 8.861$ and $\rho_{Nb} \approx 8.510$. We use these densities as the input parameters of the layered case.

For the homogeneous case, we used the effective elastic constants from Table 6.1, and we used our measured density of about 8.685 g/cm^3.

We calculated the resonance frequencies using both the interpolation basis and the power series basis, and we present our results in Table 3.8. We find moderate agreement between the homogenization and the layered system. In some modes, there is agreement on the order of 5 significant figures for the resonance frequencies. We consider this as motivation for us to use the homogeneous power series basis to model sample 1 which contains 12 layers.

Table 3.8: Resonance frequencies of Cu/Nb sample 1 were estimated using the interpolation basis and the power series basis. N = 12 was used as a truncation. For the interpolation, we used 3 sublayers inside of each material layer for L = 36. Frequencies are presented in units of kHz. The interpolation basis assumed isotropic layers. The power series basis used the homogenization from composite theory (transversely isotropic symmetry). The input elastic constants are presented in Table 6.1.

Mode	Layered Interpolation $x^l y^m \Phi_n(z)$	Homogenized Power Series $x^l y^m z^n$	Percentage Difference
1	7.365	7.367	0.027%
2	10.958	10.960	0.018%
3	14.361	14.359	−0.014%
4	18.599	18.610	0.059%
5	19.172	19.183	0.057%
6	32.624	32.631	0.021%
7	33.494	33.501	0.021%
8	35.176	35.184	0.023%
9	36.193	36.201	0.022%
10	41.941	41.942	0.002%
11	53.181	53.309	0.241%
12	54.257	54.379	0.225%
13	57.016	57.016	0.000%
14	59.889	59.890	0.002%
15	59.901	59.906	0.008%
16	63.584	63.585	0.002%
17	64.390	64.389	−0.002%
18	65.374	65.480	0.162%
19	65.692	65.692	0.000%
20	69.290	69.405	0.166%
21	74.908	74.908	0.000%
22	75.042	75.081	0.052%
23	78.679	78.710	0.039%
24	83.820	83.844	0.029%
25	89.751	89.751	0.000%
26	91.597	91.597	0.000%
27	91.806	91.806	0.000%
28	94.212	94.369	0.167%
29	96.888	96.919	0.032%
30	99.620	100.325	0.708%
31	102.518	102.953	0.424%
32	102.667	103.641	0.949%
33	105.488	105.518	0.028%
34	106.528	106.527	−0.001%

Chapter 4

Mode Identification

One of the important but difficult aspects of RUS is the part of conducting mode identification. When a RUS spectrum is measured, not all of the peaks are always visible, and they are not always the same size. We obtain a list of measured resonance frequencies, $\{g_1,g_2,g_3,...\}$, but we generally do not know beforehand if we have collected all of the resonances in a given range. Sometimes the resonance has a node at the corner touching the transducer, and this can lead to a low-amplitude peak that can be missed in the measurements.[8] We also have a list of calculated resonance frequencies, $\{f_1,f_2,f_3,...\}$, but we need to know which f_i corresponds to each g_i. In other words, when we perform our measurements, we obtain the values of multiple g_i, but we need to find out the value of the mode indices i.

One common approach to conducting the mode identification is the manual approach. This consists of taking the list of measured reasonances as well as the list of calculated resonances from the direct code, and then trying to match them up in pairs while considering the possibility that the list of measured resonances may be incomplete. Then, the sample is repositioned and the spectrum is measured again to look for any missing modes, and this process is repeated. While it is possible to achieve the mode identification in this manner, it is not always easy. Generally, the starting elastic constants should be relatively close to the actual values. If the guess elastic constants are far from the actual values, then the calculated spectrum may not resemble the measured spectrum. In [7], Migliori presents an example where

they had incorrectly matched the modes because one measured resonance frequency was missed. When they performed the fitting routine for the elastic constants, they obtained an rms error of 1.3927%. After examining the resonances and noticing that a mode was missing, they repeated the fit and this time the rms error decreased to 0.1028%. However, this technique is not always as successful as it was in Migliori's case.

Ogi and coworkers in Japan were working to determine the elastic constants of an isotropic sample of aluminum. They had measured 42 resonance frequencies. However, when Ogi used the manual approach and ran the fitting routine, the calculations didn't converge properly to values for the elastic constants. Instead, they developed an experimental solution to this problem.[21] They changed the experimental setup and added a laser interferometer so that they could measure the actual displacement at different points along the surface of the sample while applying a particular resonance frequency, thereby obtaining a picture of the mode shape. They calculated the displacement fields using the eigenvectors from the direct code, and then compared with the measured displacement fields. They found that the displacement fields corresponded very well, independent of what starting values they chose for their elastic constants, and they used this for their mode identification. Afterwards, they obtained a very precise measurement of the elastic constants of aluminum.

We do not have the experimental setup to measure the mode shapes, so the experimental solution is not accessible to us. We are studying rolled Cu/Nb samples with large interface area-to-volume ratios. Although we have estimates of what we think the elastic constants could be based on simulations we have performed, we do not have certainty about our estimates. If our initial elastic constants are far from the actual values, then our mode identification is likely to be invalid. So our system presents a problem with the manual approach as well. In an attempt to resolve this, we have developed and tested a numerical approach to mode identification. This is partially a brute-force technique. In this chapter, we present some of the details of this technique, along with simulations to assess the validity of it.

4.1 Numerical Technique: Testing Combinations

4.1.1 Limitations of Brute-Force Approach

Our numerical approach consists of simply testing combinations of measured and calculated resonances. For each of those combinations, we determine a parameter, such as the sum of squared residuals (SSR) or the RMS error. Finally, we choose the combination with the lowest value of that parameter to be our mode identification. If we have N calculated resonance frequencies and K measured resonance frequencies, then the total number of combinations is given by the following expression.

$$\binom{N}{K} = \frac{N!}{K!(N-K)!} \tag{4.1}$$

In an isotropic sample, it is recommended for there to be at least 10 measured resonance frequencies in order to achieve a fit of the elastic constants.[5] To test this approach we used a hypothetical system containing 10 measured resonance frequencies and 15 calculated frequencies. This technique accessed the 3003 combinations and it matched the modes properly.

However, this technique is very limited, and beyond this case it becomes difficult to access all of the combinations. We used the Matlab function *nchoosek* to construct the list of combinations. However, Matlab advises that if the larger array (in our case the list of calculated resonances) has more than 15 values, then the use of *nchoosek* is no longer practical. If we were to perform orthotropic fits, we should have at least 45 resonance frequencies to fit for 9 elastic constants.[5] Our experimental setup has a problem where the transducer generally does not work well below 15 kHz, so causes us to automatically miss the first 15 or 20 modes of the system. If we were to try this numerical technique using 60 calculated resonance frequencies and 45 measured resonance frequencies, then it would involve over $5.3\text{x}10^{13}$ combinations, which is more than the computational capacity of our computers can handle. For this, we adapt the technique so that we only access a portion of all of the available combinations.

4.1.2 Identifying Batches

When people perform the manual approach, they generally compare groups of measured resonance frequencies with groups of calculated resonance frequencies. We use the same idea here but we automate the approach so that it can be done numerically.

We start by matching the lowest modes first. However, a key detail here is that we cannot match modes one by one. I think the best way to illustrate this is with an example. Suppose we have a hypothetical system whose resonance frequencies are displayed in Table 4.1.

Table 4.1: A set of hypothetical measured and calculated resonance frequencies are presented, along with their mode numbers.

Mode	Measured Freq.	Calculated Freq.
1	1.20	1.10
2	2.10	2.20
3	3.70	3.30
4	3.90	3.50
5	4.25	4.20
6	5.10	5.05
7	6.75	6.80
8	6.85	6.90
9	6.99	7.00
10	7.40	7.50
11	8.10	8.00
12	8.90	9.00

However, we do not actually know beforehand the mode identifications, the column labeled "Mode". If we start matching the measured resonances one by one, by simply identifying the nearest calculated modes, then we would match the first two correctly. We would identfy the measured 1.2 kHz resonance with the calculated 1.1 kHz resonance. Similarly for the measured 2.1 kHz reosnance and the calculated 2.2 kHz resonance. However, if we use this approach on the 3rd mode, then we would incorrectly match the measured 3.7 kHz resonance with the calculated 3.5 kHz resonance. In other words, we would inadvertently call the 3.7 kHz resonance, the "4th mode". This effect then propagates through the rest of the list and can repeat itself. We would call the 3.9 kHz resonance the "5th mode", while the 4.25 kHz resonance the "6th mode", and so on. Matching modes one-by-one can lead to an incorrect

mode identification. We display this in Fig. 4-1a. A solution here is to batch the resonances into groups.

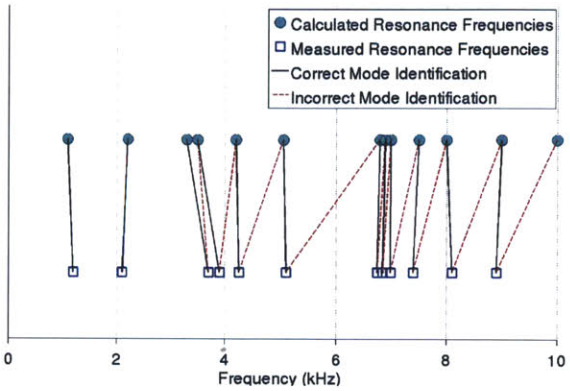

(a) The set of measured and calculated resonances are presented along with the correct mode identification (black). Performing the mode identification with one measured resonance at a time yields incorrect results (red).

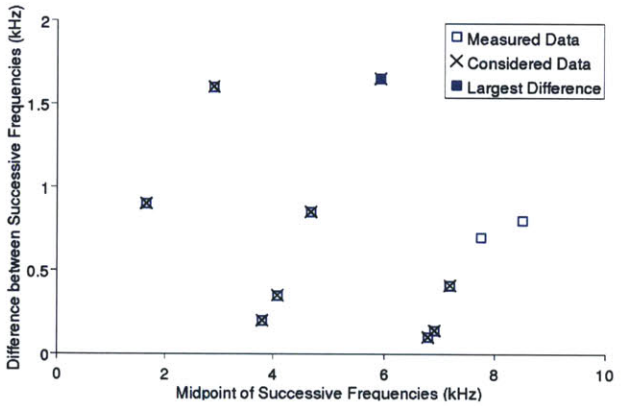

(b) The differences between successive measured resonance frequencies is plotted as a function of the midpoints. The point with the largest difference (shaded blue) corresponds to the large gap between the 6th and 7th modes.

Figure 4-1: The set of hypothetical resonances from Table 4.1 is used in this simulation to present the problem of a one-by-one mode identification (top), and the solution of identifying a batch size (bottom).

Since it is not feasible for us to match all modes simultaneously, and matching one by one is inaccurate, then we group the measured frequencies into batches. Some questions may arise here: what is the size of the batches and is the size constant? Our answer is that we allow the size of the batches to vary, because otherwise, the problem

remains present. For instance, if we reconsidered the example we were studying in Table 4.1, and we collected the lowest 12 calculated resonances and we wanted to match the lowest 3 modes simultaneously, then the third mode would still be matched incorrectly. This problem can occur at the low modes and also at the high modes. Whether or not it occurs depends on how close the resonances are to each other. If the resonances are far apart, then this problem is less likely to occur. For this, we allow the size of our batches to depend on the differences between successive resonances.

We start by taking an initial list of measured resonance frequencies, such as the first 10 in Table 4.1. We consider successive resonances and their differences as functions of their midpoints in Fig. 4-1b. We select the point with the maximum successive difference and we take its midpoint to be the upper bound for our group of measured resonance frequencies. In the example we have been considering, we find the maximum successive difference to have a midpoint of 5.925 kHz. Based on this, we take the 6 resonances below this frequency to be our measured group.

Next, we need to select a group of calculated resonance frequencies. For this, we look at our measured group of resonance frequencies and identify the mean μ of the resonances. Then, we choose the 15 calculated resonance frequencies that are closest to μ as our group of calculated resonance frequencies.

Finally we take our measured group and our calculated group of resonances, and we access all possible combinations between them. We choose the one with the minimum SSR as the mode identification for this group of measured resonances. We finish by removing the set of measured resonances and their corresponding matched calculated resonances from the original lists, and we repeat this process with the next set of measured and calculated groups. This approach yields the correct mode identication displayed in Fig. 4-1a. In our codes, we often considered up to 10 measured frequencies and 15 calculated frequencies at a time. However, we also tried to test the limitations of the computer we were using and we found that using this approach of *nchoosek* with batches of 10 measured frequencies and 28 calculated frequencies can work successfully in just a few minutes.

4.2 Simulations

To test our numerical mode identification, we conduct a series of simulations. We assume a hypothetical isotropic material whose elastic constants are $C_{11} = 2.0$ and $C_{44} = 0.4$ x 10^{12} dynes/cm^2. We also assume it to be a homogeneous material with the geometry of sample 2: where its dimensions are 3.161 x 1.006 x 0.03002 cm^3. The mass is 0.8150 g. We calculate the resonance frequencies of this homogeneous material, and present them as the "original" frequencies in Table 4.2.

For our first simulation we treat these "original" frequencies as if they were a set of measured frequencies, and we access different points in the parameter space of C_{11} and C_{44} to obtain sets of calculated resonance frequencies to use for our mode identifications.

For our second simulation, we take the "original" frequencies, and shift them by a random amount of noise of up to $\pm 2.5\%$. In some cases the ordering of the resonances changes, so we need to sort them again, and we present these resonances as the "resorted" resonances in Table 4.2. We take the "resorted" frequencies to be the measured frequencies, access different points in the parameter space, and implement mode identifications.

The idea in both of these cases is that we are assuming we do not know beforehand the information from the column labeled "Mode" in Table 4.2. Instead, we are trying to deduce it using our numerical approach.

Table 4.2: A hypothetical system was used with the geometry of sample 2. The mass and geometry correspond to sample 2. This simulation was performed using our direct code. $N = 20$ was used with the power series basis for this simulation.

Mode	Original Frequency	Random Error (%)	Modified Frequency	Resorted Frequency
1	1.115	0.071	1.116	1.116
2	2.063	1.810	2.100	2.100
3	3.105	−0.140	3.101	3.101
4	4.363	0.942	4.404	4.404
5	6.122	2.204	6.257	6.257
6	7.116	−1.220	7.029	7.029
7	10.058	−0.336	10.024	10.024
8	10.520	0.294	10.551	10.551
9	11.602	−1.536	11.424	11.424
10	12.501	−0.728	12.410	12.410
11	14.238	−0.296	14.196	14.196
12	14.721	0.900	14.854	14.854
13	15.777	0.330	15.829	15.829
14	17.754	−0.813	17.610	17.610
15	19.825	0.937	20.011	20.011
16	21.693	0.297	21.757	21.757
17	21.964	1.112	22.208	22.208
18	25.814	1.320	26.155	26.155
19	26.954	2.167	27.538	27.538
20	28.792	−0.570	28.628	28.364
21	28.802	−1.521	28.364	28.628
22	31.508	0.117	31.545	31.545
23	32.474	1.231	32.874	32.274
24	32.709	1.079	33.062	32.874
25	33.081	−2.438	32.274	33.062
26	34.916	1.607	35.477	35.477
27	36.923	0.346	37.051	37.051
28	37.524	−1.224	37.065	37.065
29	39.317	2.242	40.198	40.198
30	41.393	1.148	41.868	41.101
31	41.941	−2.004	41.101	41.868
32	45.987	−1.111	45.476	45.476
33	46.756	2.261	47.813	46.538
34	47.237	−1.480	46.538	47.813
35	50.405	2.278	51.553	51.553
36	53.501	−2.144	52.354	52.354
37	55.046	−1.656	54.135	54.135
38	56.404	−1.575	55.515	55.261
39	56.413	−2.042	55.261	55.515
40	59.631	−2.291	58.265	58.265
41	59.794	−1.999	58.599	58.599
42	61.233	0.733	61.682	60.464
43	61.845	−2.234	60.464	61.664
44	62.654	−1.580	61.664	61.682
45	63.840	2.448	65.402	64.248
46	65.106	−1.318	64.248	65.402
47	67.420	−1.935	66.116	66.116
48	68.154	1.571	69.225	68.064
49	68.235	−0.250	68.064	69.225
50	71.719	1.108	72.514	72.514

Performing Mode Identification using Original Frequencies

For our first simulation, we take the set of green original frequencies from Table 4.2 to be our set of "measured" frequencies. This simulation is supposed to represent an ideal situation where the resonance frequencies were measured exactly. We choose to consider the 11th through 50th resonances. We start with the 11th resonances in order to see if our approach can work for the cases where we do not know what the first resonances are. In addition to that, our experimental setup has problems below 15 kHz, so in our measurements we generally are not capable of identifying the first resonances.

For our set of calculated resonances, we begin accessing different points in the parameter space. We consider 31 distinct values of C_{11} between 1.0 and 3.0. We consider 31 distinct values of C_{44} between 0.2 and 0.4. This provides a total of 961 points in the parameter space of C_{11} and C_{44}. At each point, we took the first 100 calculated resonance frequencies and we then applied the mode identification with our set of 40 "measured" resonances. Additionally, we computed the SSR and RMS error for each mode identification. These simulation results are presented in Fig. 4-2 and 4-3.

Both the SSR and the RMS error have a minimum at $C_{11} = 2.00$ and $C_{44} = 0.40$, which is consistent with what is expected. The RMS error exhibits a minimum that is better defined than the SSR. In the contour plot of Fig. 4-2a, the composite function varies more quickly with C_{44} than with C_{11}. This is consistent with the literature, as it is generally easier to measure C_{44} than C_{11}.[6] Another feature is that both the RMS and SSR landscapes do not appear to be differentiable. This results from how different regions have different mode identications. When a fitting routine is performed for the actual parameters, the mode identification is held constant, and the landscape of the composite function is expected to be smooth with a better-defined minimum. During this searching routine, we expect the minimum to be more shallow, because areas that are farther away from the minimum have a lower SSR and RMS than they would otherwise because of their distinct mode identification.

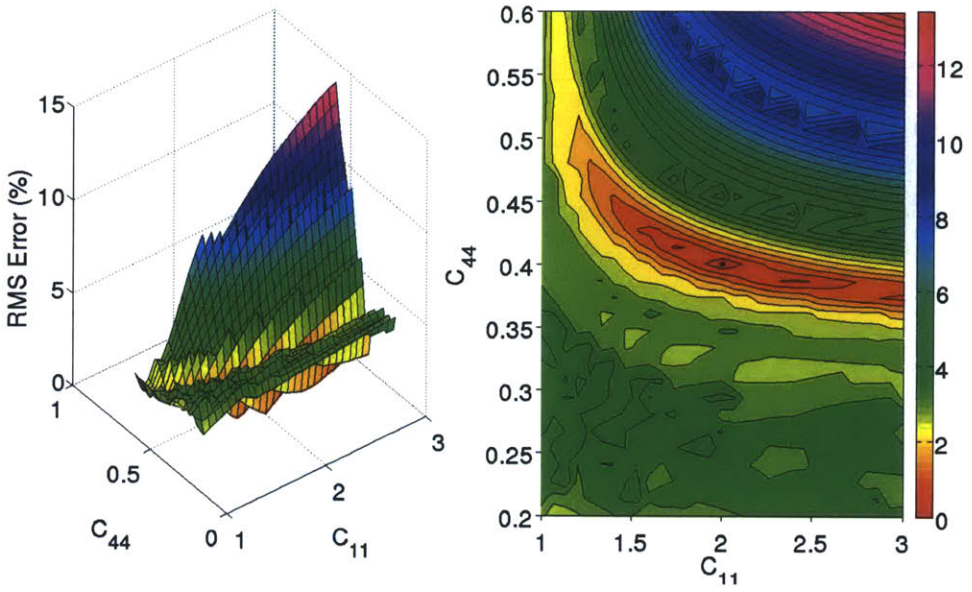

(a) RMS error from Original Frequencies

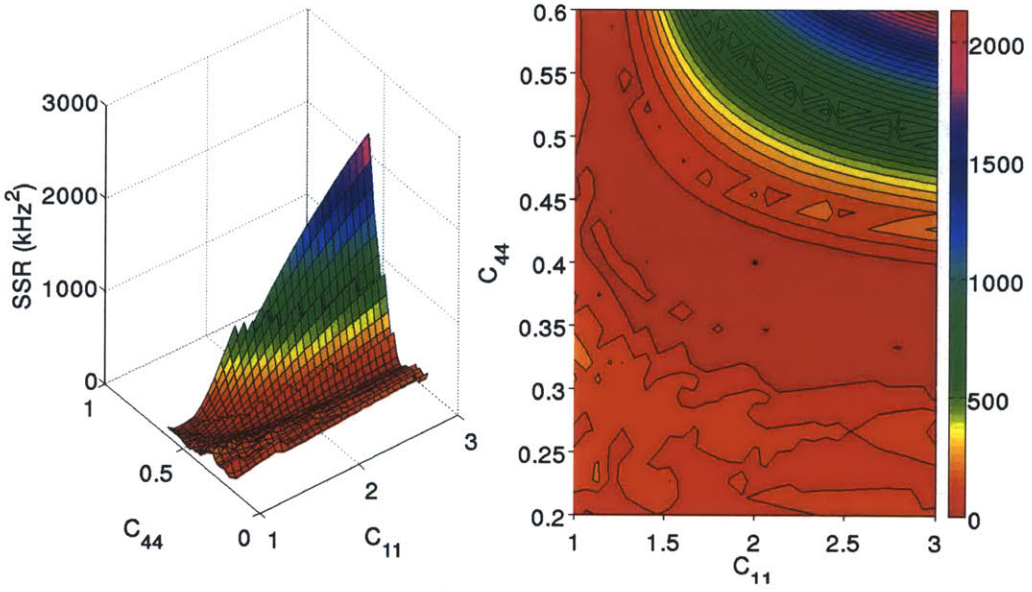

(b) SSR from Original Frequencies

Figure 4-2: A simulation was conducted using the original green resonance frequencies from Table 4.2. A total of 961 distinct sets of calculated resonance frequencies were tested. The point with the minimum RMS error ($C_{11} = 2.0000$ and $C_{44} = 0.4000$) is labeled with a black dot.

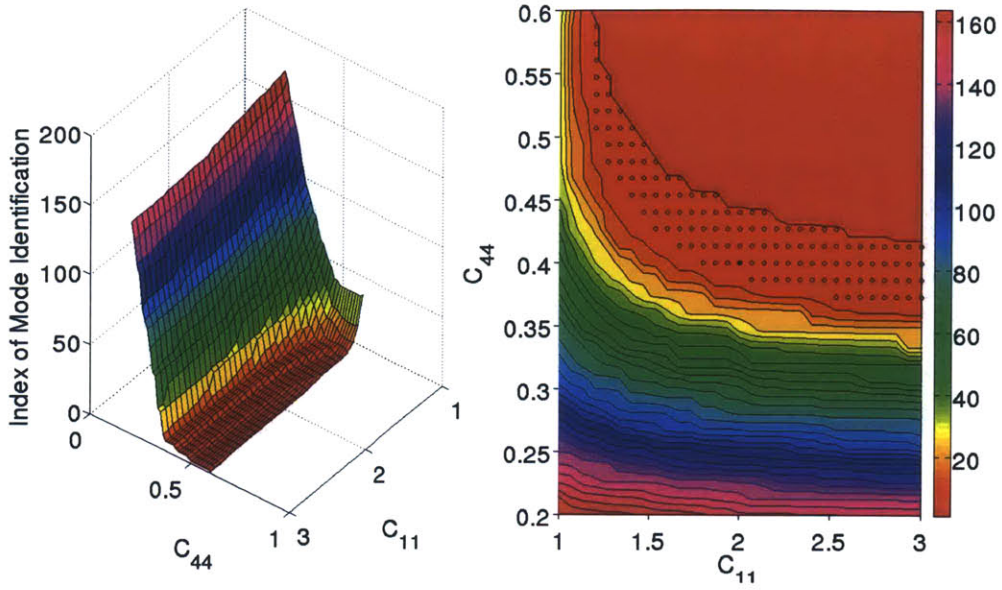

(a) Distinct mode identifications using original frequencies are presented. The point with the minimum RMS error is labeled with a black dot. The points with the same mode identifications as the minimum were labeled with light circles.

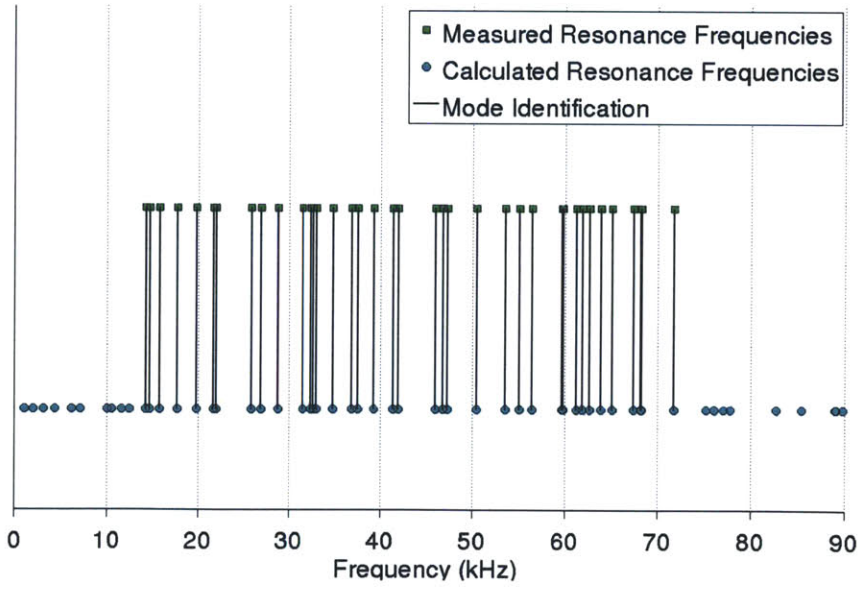

(b) Mode Identification of Minimum using Original Frequencies

Figure 4-3: A simulation was conducted using the original green resonance frequencies from Table 4.2. The band of points with the same mode identifications illustrate a region of stability for this approach (top). The correct mode identification was achieved (bottom).

In Fig. 4-3 we present results on the mode identifications for this simulation. We refer to a mode identification as the list of values that would correspond to the first column in Table 4.2 using our approach. At each point in the parameter space a mode identification was recorded. Generally, multiple points would have the same mode identification or list. We found there to be approximately 160 distinct mode identifications. For each distinct list, we assigned a value that we call an "Index" in Fig. 4-3a. There is no physically significance to the value itself. What has significance is the distribution of a given value throughout the parameter space. In Fig. 4-3b, we show the mode identification at the minimum point, and it is consistent with the first column in Table 4.2. In Fig. 4-3a, a series of unfilled circles are used to label the points that have the same mode identification as the minimum. If there is a large number of these unfilled circles in the parameter space, then the mode identification of the minimum tends to be more stable.

Performing Mode Identification using Frequencies with $\pm 2.5\%$ Noise

For our second simulation, we take the set of blue resorted frequencies from Table 4.2 to be our set of "measured" frequencies. This simulation is intended to model a more realistic situation than the previous one, as here we consider the existence of up to 2.5% noise in the measurements. Similarly, we consider the 11th through 50th resonances.

For our set of calculated resonances, we use the same 961 points in the parameter space of C_{11} and C_{44} as in the previous simulation. At each point, we took the first 100 calculated resonance frequencies and we then applied the mode identification with our set of 40 "measured" resonances. We present these simulation results in Fig. 4-4 and 4-5.

The RMS error landscape of this simulation was found to have a global minimum at $C_{11} = 1.9333$ and $C_{44} = 0.4000$. This is relatively accurate compared to the starting values. The RMS error exhibits a fairly defined minimum, while the SSR appears to be quite ill-defined in terms of its contour. However, it is important to note that when we compare Fig. 4-4 to Fig. 4-2, the minimum of the composite function of this simulation with noise is less well-defined.

In Fig. 4-3 we present results on the mode identifications for this simulation. We find from Fig. 4-5b that the minimum point in this simulation has the same mode identification as in the simulation without noise, and it is also consistent with the first column in Table 4.2. From Fig. 4-5a, we find that a considerable amount of nearby points in the parameter space also had the same mode identification.

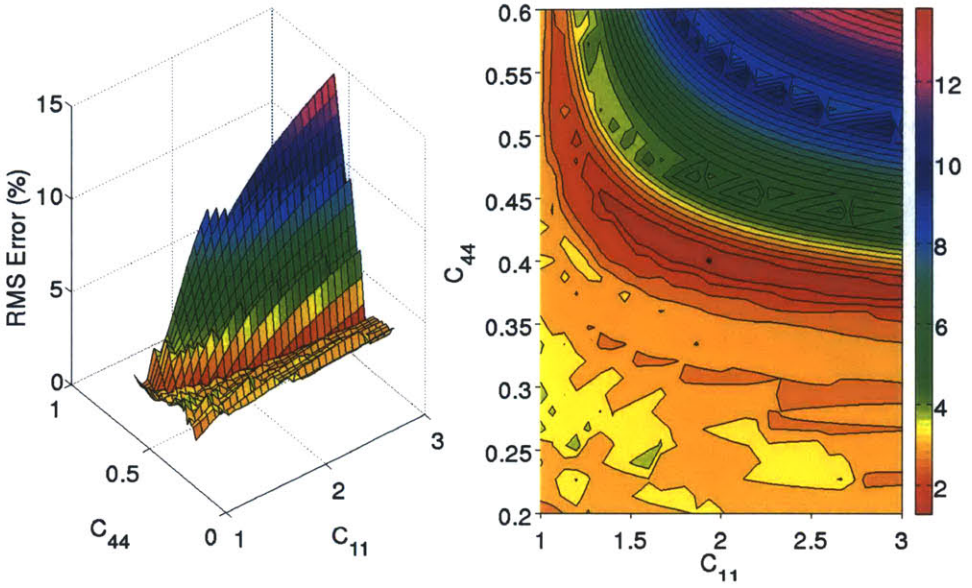

(a) RMS error from Frequencies with ±2.5% Noise

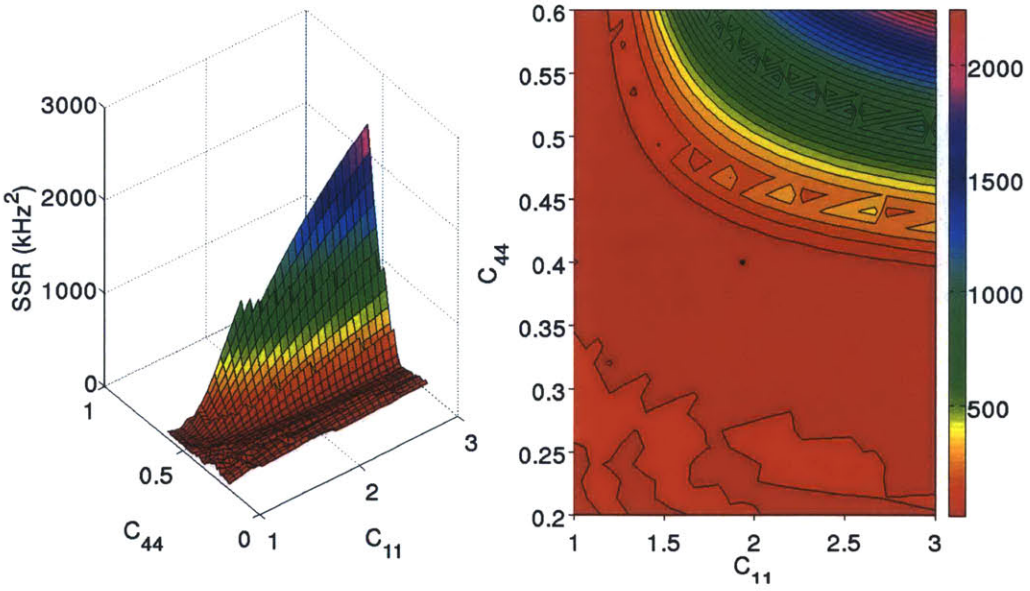

(b) SSR from Frequencies with ±2.5% Noise

Figure 4-4: A simulation was conducted using the blue resonance frequencies from Table 4.2 that contain the effects of ±2.5% noise. A total of 961 distinct sets of calculated resonance frequencies were tested. The point with the minimum RMS error ($C_{11} = 1.9333$ and $C_{44} = 0.4000$) is labeled with a black dot.

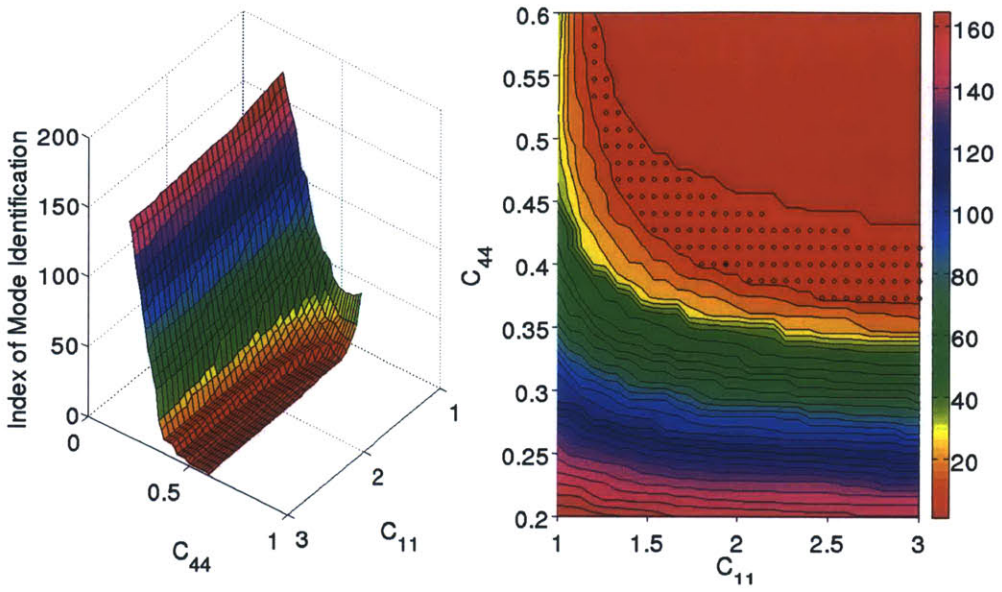

(a) Distinct mode identifications using modified frequencies are presented. The point with the minimum RMS error is labeled with a black dot. The points with the same mode identifications as the minimum were labeled with light circles.

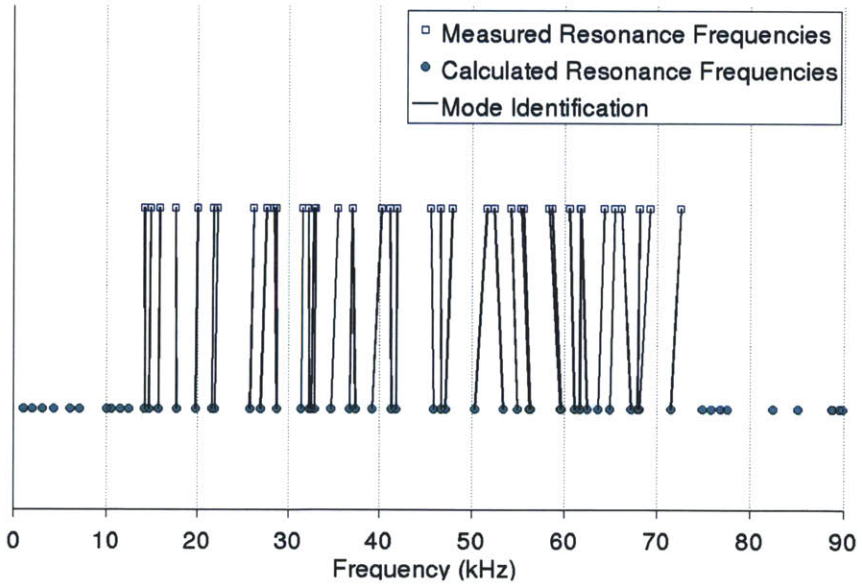

(b) Mode Identification of Minimum including ±2.5% Noise

Figure 4-5: A simulation was conducted using the modified blue resonance frequencies from Table 4.2 that contain the effects of ±2.5% noise. The band of points with the same mode identifications illustrate a region of stability for this approach (top). The correct mode identification was achieved (bottom).

Problems that Occured in Other Cases

In these two simulations, this numerical approach appears to have been successful as it yielded the correct mode identification in both cases. However, this was not always the case. For example, we tried conducting these simulations using only 20 measured resonance frequencies and up to $\pm 5\%$ noise, but we found that the results were not very accurate for the noise simulation as the minimum would appear at $C_{11} = 1.7333$ and $C_{44} = 0.4133$, and its mode identification was not correct. However, the Master's Thesis of María Teresa Cerda Guevara has simulations where she explains that the use of a higher amount of resonances increases the accuracy when identifying the minimum of the composite function.[17] Based on this, we increased the number of "measured" resonances to 40. Nevertheless, with the simulation of $\pm 5\%$ noise, we were unable to obtain presentable results. As a result of this, our numerical approach is limited when there is a small number of measured resonances or when there are considerable inaccuracies in the measurements.

Chapter 5

Theory of Inverse Code in RUS

5.1 Objective Function

The fitting routine for determining the elastic constants in RUS is often refered to as the "inverse code" or the "inverse problem" in the literature.[6] This process consists of varying the input elastic constants in order to improve the agreement between the measured and calculated resonance frequencies. The set of measured frequencies is denoted by g and the set of calculated frequencies is denoted by f. In RUS, the following objective function, F, is chosen for the fitting routine.

$$F = \sum_i w_i \left(f_i - g_i\right)^2 \tag{5.1}$$

w_i is defined to be a weighting factor. When a mode is omitted from the fitting routine, its value is zero. Otherwise, w_i takes the value g_i^{-2}. As a result, F is proportional to the RMS error between the calculated and measured resonance frequencies. It may be important to highlight that it is preferable to use F or the RMS error as the objective function as oppose to the sum of squared residuals, SSR. In our simulations in Fig. 4-2 and Fig. 4-4 it is evident that the minimum of the objective function is better defined in the case of the RMS error than in the case of the SSR.

5.2 Levenberg-Marquardt Algorithm

The program rpr.exe that was prepared by Migliori is capable of solving the inverse problem.[16] Their code implements the Levenberg-Marquardt algorithm to minimize the objective function. Here we elaborate on the formalism as it is explained in [6].

To start off, the objective function F is viewed as a function of a set of input parameters $\vec{x}$. The set of starting parameters (in our case the initial values of the elastic constants) are defined as the components of $\vec{x}_0$. M is defined to be the number of input parameters or the number of dimensions of $\vec{x}$. If the initial parameters are relatively close to the actual values, then it is safe to approximate F using the first terms of a Taylor series expansion about $\vec{x}_0$.

$$F(\vec{x}) = F(\vec{x}_0) + \sum_{\alpha\beta} \left[[x - x_0]_\alpha \left[\frac{\partial F(x_0)}{\partial x_\alpha} \right] + \frac{1}{2} [x - x_0]_\alpha \left[\frac{\partial^2 F(x_0)}{\partial x_\alpha \partial x_\beta} \right] [x - x_0]_\beta \right] \quad (5.2)$$

The first term in brackets corresponds to the terms of the gradient of $F(\vec{x}_0)$, while the second term in brackets corresponds to the terms of the Hessian matrix of $F(\vec{x}_0)$.

By setting $\vec{x}$ to be the vector of fit parameters that minimize F, the following set of equations are formed.

$$\frac{\partial F(x_0)}{\partial x_\alpha} + \sum_\beta \left[\frac{\partial^2 F(x_0)}{\partial x_\alpha \partial x_\beta} \right] (x - x_0)_\beta = 0, \qquad \alpha = \{1, 2, ..., M\} \quad (5.3)$$

To solve these M equations for the M components of $\vec{x}$, we need the components of the gradient and the Hessian matrix of F. Their analytical solutions are:

$$\frac{\partial F}{\partial x_\alpha} = 2w_i (f_i - g_i) \frac{\partial f_i}{\partial x_\alpha} \quad (5.4)$$

$$\frac{\partial^2 F}{\partial x_\alpha \partial x_\beta} = 2w_i \frac{\partial f_i}{\partial x_\alpha} \frac{\partial f_i}{\partial x_\beta} + 2w_i (f_i - g_i) \frac{\partial^2 f_i}{\partial x_\alpha \partial x_\beta} \quad (5.5)$$

According to [6], the second term in Eq. 5.5 can be dropped for a variety of reasons. One reason is that it is expected to be small in magnitude. We now assign $\vec{B}$ to be

the gradient vector and $\boldsymbol{A}$ to be the Hessian matrix.

$$B_\beta = w_i \left(f_i - g_i\right) \frac{\partial f_i}{\partial x_\beta} \tag{5.6}$$

$$A_{\alpha\beta} = w_i \frac{\partial f_i}{\partial x_\alpha} \frac{\partial f_i}{\partial x_\beta} \tag{5.7}$$

In order to implement the fitting routine, the components of $\vec{x}$ change depending on how far the initial value is from the minimum of the composite function. If the minimum is far away, then the parameters change in the direction of steepest descent. If its parameters are close, then the change considers the components of the Hessian matrix as well.

$$x_\alpha = \begin{cases} x_{0\alpha} - A^{-1}_{\alpha\beta} B_\beta & \text{if } x_\alpha \text{ is close to the minimum} \\ x_{0\alpha} - \text{constant} * B_\alpha & \text{if } x_\alpha \text{ is far from the minimum} \end{cases} \tag{5.8}$$

In order to go from one case to the other, the rpr.exe code uses a dimensionless parameter Ω. With this parameter, a matrix $\boldsymbol{G}$ is defined and its elements take the place of the coefficients of the second terms in Eq.5.8. The two equations that are used to identify successive values in x_α are:

$$x_\alpha = x_{0\alpha} - G_{\alpha\beta} B_\beta \tag{5.9}$$

$$G^{-1}_{\alpha\beta} = A_{\alpha\beta} \left(1 + \Omega \delta_{\alpha\beta}\right) \tag{5.10}$$

Ω is initially set to a large value. As Ω varies from a large value to 0, the system changes from the second case in Eq. 5.8 to the first case.

To obtain uncertainties on the fit parameters, Migliori's code uses the eigenvalues and eigenvectors of $\boldsymbol{G}$ to identify a percentage change in each parameter about the minimum that would correspond to a change of 2% in F.[6]

Chapter 6

Data Analysis

6.1 Problem at Small Layer Widths: Existence of Multiple Minima

In [6], Migliori explains that errors in the geometry and missed modes can lead to the development of multiple minima in the objective function. In our measurements, we have observed this problem, particular in the samples with smaller layer widths, samples 2 and 3. For sample 1, we present a set of fits from different starting parameters in Table 6.4, and we observe that the majority of the fits converge to the same values. For the other samples, we present some of our fits in Tables 6.7 and 6.10 and the majority of these fits diverged from each other, or converged to different values for their elastic constants. This feature was expected to be observed in the smaller layer widths because of our greater uncertainty in the mode identification (the larger number of missed modes) compared to sample 1, and for this we took several measures in attempts to improve our fits. We performed a parameter space search to look for minima in the objective function, we also attempted to perform a texture analysis in order to help improve the starting parameters, and we sought to improve the mode identification by including estimates of resonances in the nonlinear regime as a representation of the missed modes. Nevertheless, the uncertainties for samples 2 and 3 were too large to achieve successful measurements of the elastic constants.

6.2 Searching of Multi-Dimensional Parameter Space

Given that we do not know the values of the elastic constants of our copper-niobium samples prior to our measurements, we searched through the multi-dimensional elastic constant space before performing the fitting routine.

For sample 1, we initially searched through 3025 points in the 4 dimensional space of isotropic layers as well as 3600 points in the 6 dimensional space of cubic layers, as we were considering the use of the layered code. We later decided to simplify our calculations by using the homogenous system for the fitting routine. For samples 2 and 3, we searched 42875 points in the 3 dimensional space of a homogeneous cubic system and 46656 points in the 9 dimensional space of an orthotropic system. For each point in the parameter space that was accessed, we calculated the resonance frequencies, compared them to our set of measured resonances and performed a numerical mode identification. We compared the calculated and measured resonances to obtain the RMS error and the SSR for each point. The point with the minimum RMS error was used as the starting point for some of the fits we conducted.

With increasing dimensionality, this approach quickly becomes limited by the factor of time. Our layered code for sample 1 took about 2 minutes for each iteration. The homogeneous codes used took under 10 seconds per iteration. This also motivated our switch from the layered code to the homogeneous code as it provided a higher speed for our calculations. However, even in the homogeneous cases, it took several days to perform the parameter space search.

6.3 Use of Texture Analysis

Carlos Tomé (LANL) has developed a visco-plactic self consistent (VPSC) code which can simulate the plastic deformation of a material. It also has the capacity to calculate the values of polycrystalline elastic constants provided a set of input monocrystalline elastic constants and a texture file. The texture is specified as a discrete set of

orientations, each containing three Euler angles and a volume fraction.

In Chapter 7 of [22], Tomé presents simulations for polycrystalline elastic constants of copper in the cases of random texture (isotropic symmetry) and also rolled texture (orthotropic symmetry). His simulations show that isotropic copper and rolled copper have close values for C_{ij}, where differences between respective elastic constants are less than 5 GPa. He explains that this is a result of the high symmetry of copper.

Although our samples have been prepared using accumulated roll bonding, we use a isotropic (random) texture to serve as a procedure for estimating the elastic constants in the layers of both copper and niobium. Our isotropic texture was prepared by using Matlab to generate a list of 1000 random orientations. We obtained the single-crystalline elastic constants of copper and niobium using [22] and [20] respectively. With VPSC, we obtained estimates on the elastic constants of isotropic copper and niobium. Our values differ from those published by Tomé in [22] and this could be a result of how we used different texture files. For the purpose of performing fits with the homogeneous code, we use the equations developed by Grimsditch to obtain the effective elastic constants.[19] The use of isotropic layers yields a transversely isotropic material. In Table 6.1, we present the results of this simulation. In subsequent sections, we present several fits for samples 1,2 and 3. In each of the samples, we take fit 1 to start near the effective elastic constants of this simulation.

Table 6.1: Estimates of the elastic constants of isotropic copper and isotropic niobium are presented. Their elastic constants were calculated using the VPSC code from Tomé. Estimates of homogeneous effective elastic constants C^{eff} are also presented.

	Monocrystalline Copper	Monocrystalline Niobium	Isotropic Copper	Isotropic Niobium	Effective Cu/Nb
C_{11}	1.680	2.465	1.9773	2.2287	2.07229
C_{22}	1.680	2.465	1.9773	2.2287	2.07229
C_{33}	1.680	2.465	1.9773	2.2287	2.09549
C_{23}	1.214	1.345	0.9817	1.4899	1.22064
C_{13}	1.214	1.345	0.9817	1.4899	1.22064
C_{12}	1.214	1.345	0.9817	1.4899	1.20512
C_{44}	0.754	0.2873	0.4978	0.36937	0.42407
C_{55}	0.754	0.2873	0.4978	0.36937	0.42407
C_{66}	0.754	0.2873	0.4978	0.36937	0.43358

6.4 Improving the Mode Identification

For each of the three samples, we collected a single measurement in the linear elasticity regime. We also collected measurements of the resonance frequencies in the nonlinear regime in an attempt to identify missing modes. Initially, when we performed the numerical mode identification, we restricted it only to the values that were measured in the linear elasticity regime. We observed that the output did not always present missing modes where we had estimates of resonances from the nonlinear regime.

To improve this, we decided to conduct the numerical mode identification by combining our resonances from multiple measurements, but for our fitting procedure, we only used the measurements in the linear elasticity regime. In Tables 6.2, 6.6, and 6.9, we show the measurements from both regimes for the three samples. For each of the missed modes in the column labeled "Measurement", we used the average of the available resonance frequencies in the nonlinear regime for the mode identification. Then, we removed that data point prior to running rpr.exe for the fitting procedure.

6.5 Sample 1: Layer Width of 0.165 mm

Sample 1 contained the largest layer width and the lowest interface area-to-volume ratio of the three samples. It also had the largest thickness in the z dimension. This provided the benefit that it had less resonances below 15 kHz, where our experimental setup is limited. We decided to start our measurements with the 6th mode, near 31.7 kHz. We present our measurements and estimates from different positions of the sample in Table 6.2. The mode identification presented corresponds to our numerical approach. Modes 30 and 32 were missed in our measurements in the linear elasticity regime.

For our fitting procedure, we used the remaining 27 modes with the code of rpr.exe from Migliori. Although the layered composite is not a cubic material, we decided to fit it using cubic symmetry as an approximation to its actual properties. Tomé explained that textured copper alone has elastic constants that are close to those of

isotropic copper.[22] We assume that the same property can be expected for niobium. We consider that although a rolled composite is expected to have orthotropic symmetry, the use of a cubic fit allows us to obtain values of the elastic constants that are close to those of an orthotropic fit. The effective elastic constants in Table 6.1 are for a transversely isotropic system, but here we use them as estimates for a cubic system by averaging set of elastic constants for C_{11}, C_{12}, and C_{44}. We use these estimates as starting parameters and present one of our fits in Table 6.3.

Table 6.2: Resonances frequencies from Sample 1 are presented in kHz. The estimates were obtained in the nonlinear regime. The measurement was obtained in the linear regime.

	Measurement	Estimated Resonance Frequency				
Mode	Position 1	Position 1	Position 2	Position 3	Position 4	Position 5
6	31.667	31.67	31.70	31.70	31.66	31.60
7	32.373	32.37	32.51	32.60	32.64	32.49
8	34.188	34.19	34.31	34.35	34.35	34.20
9	34.964	34.97	34.97	34.95	34.95	34.96
10	41.069	41.07	41.31	41.44	41.39	41.14
11	50.751	50.75	50.89	50.89	50.88	50.85
12	51.958	51.95	52.16	52.22	52.20	52.06
13	53.976	53.98	54.21	54.21	54.24	54.23
14	57.761	57.77	57.68	57.70	57.69	57.65
15	58.386	58.39	58.40	58.47	58.40	58.32
16	61.686	61.69	61.81	61.84	61.84	61.73
17	62.860	62.86	62.99	—	63.04	62.91
18	63.307	63.31	63.35	—	63.33	63.29
19	64.474	64.47	64.33	64.29	64.33	64.32
20	66.733	66.73	66.91	66.95	66.99	66.84
21	71.256	71.25	71.49	71.58	71.50	71.45
22	73.854	73.86	73.83	73.89	73.86	73.74
23	74.977	74.98	75.09	75.10	75.06	75.06
24	80.137	80.14	80.41	80.52	80.45	80.31
25	85.696	85.70	85.84	85.84	85.89	85.85
26	88.859	88.86	88.93	88.94	88.97	88.92
27	89.320	89.32	89.43	89.40	89.45	89.45
28	90.513	90.51	90.41	90.42	90.39	90.42
29	93.144	93.15	93.04	—	93.05	93.00
30	—	—	94.82	94.81	94.82	94.81
31	97.005	97.04	97.27	97.29	97.33	97.25
32	—	97.91	98.14	98.22	98.18	98.12
33	101.129	101.12	101.29	101.38	101.35	101.21
34	102.222	102.22	102.50	102.50	102.51	102.39

Table 6.3: A fit of the resonance frequencies from sample 1 is presented. It was performed using rpr.exe with $N = 18$. The input parameters were estimates based on the effective elastic constants from the VPSC simulation.

Iteration	C_{11}	C_{12}	C_{44}	RMS Error
Initial	2.080	1.210	0.430	3.9893 %
1	2.049	1.238	0.392	0.9551 %
2	1.681	0.840	0.389	0.7429 %
3	1.630	0.767	0.389	0.5757 %
4	1.634	0.771	0.389	0.5746 %
5	1.634	0.771	0.389	0.5746 %
6	1.634	0.771	0.389	0.5746 %
Final	1.634 ± 0.024	0.771 ± 0.028	0.389 ± 0.002	0.5746 %

We performed 4 other fits from different starting points to assess the stability of this fit. Fit 2 started near the minimum, while fits 3,4, and 5 had starting points that were chosen arbitrarily. We used the same mode identification for each of these fits and we present them in Table 6.4. We find that in the majority of the cases, there was a convergence to the same set of elastic constants. Fit 3 yielded a different set of fit parameters with a larger rms error and a higher uncertainty in C_{11} and C_{12}. We think that Fit 3 encountered a second minimum in the objective function, but that the other fits are more representative of the elastic constants of the system.

Table 6.4: A portion of the fits that were performed with sample 1 are presented. Fits were performed using rpr.exe with $N = 18$ and all fits presented took less than 25 iterations. All fits had the same mode identification.

Fit	Label	C_{11}	C_{12}	C_{44}	RMS
1	Initial	2.08	1.21	0.43	3.9893 %
	Final	1.63 ± 0.02	0.77 ± 0.03	0.389 ± 0.002	0.5746 %
2	Initial	1.6373	0.7750	0.3892	0.5750 %
	Final	1.64 ± 0.02	0.78 ± 0.03	0.389 ± 0.002	0.5746 %
3	Initial	2.0	1.0	0.4	5.9739 %
	Final	2.11 ± 0.07	1.29 ± 0.07	0.374 ± 0.002	0.7545 %
4	Initial	0.8	0.6	0.4	35.5469 %
	Final	1.63 ± 0.02	0.77 ± 0.03	0.389 ± 0.002	0.5746 %
5	Initial	3	2	0.8	23.2356 %
	Final	1.63 ± 0.02	0.77 ± 0.03	0.389 ± 0.002	0.5746 %

We also performed other tests that we do not present here. In our mode identification from Table 6.2, we found there to be 2 missing modes (30 and 32). We tried changing the locations of their resonances (the mode numbers of the missing modes), and performed multiple fits to see how the results would change. In all cases, the uncertainties on the parameters were greater than or equal to those from Table 6.3 and the rms error was higher. Based on these results we consider to have achieved a successful fit for the elastic constants of sample 1.

We present a graphical representation of our fit in Fig. 6-1. We also present the resonance frequencies of our fit parameters in Table 6.5.

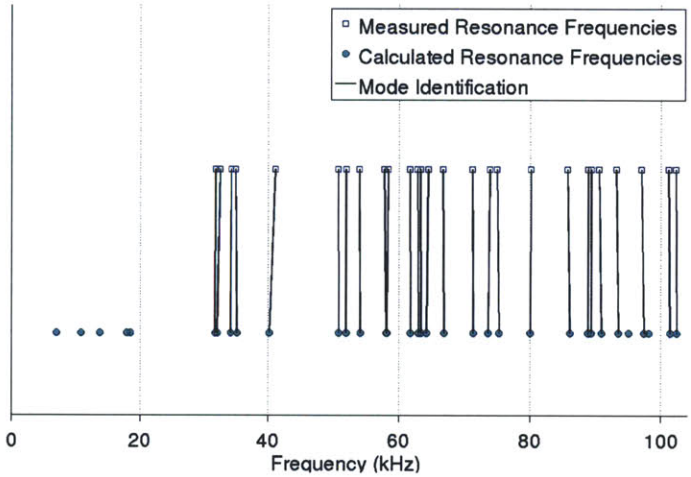

Figure 6-1: The measured resonance frequencies of sample 1 along with the calculated resonances of the fit parameters and their mode identifications are presented.

Table 6.5: The results from fit 1 of sample 1 are presented. The input parameters were $C_{11} = 1.63$, $C_{12} = 0.77$, and $C_{44} = 0.389$. The rms error was 0.5746%.

Mode	Measured Freq.	Calculated Freq.	% Error
1	—	6.989	—
2	—	10.852	—
3	—	13.777	—
4	—	17.865	—
5	—	18.447	—
6	31.667	31.595	−0.23
7	32.373	31.924	−1.39
8	34.188	34.079	−0.32
9	34.964	35.173	0.60
10	41.069	40.194	−2.13
11	50.751	50.826	0.15
12	51.958	51.926	−0.06
13	53.976	54.084	0.20
14	57.762	58.095	0.58
15	58.386	58.187	−0.34
16	61.686	61.781	0.15
17	62.860	63.026	0.26
18	63.307	63.398	0.14
19	64.474	64.238	−0.37
20	66.733	66.885	0.23
21	71.256	71.386	0.18
22	73.854	73.643	−0.29
23	74.977	75.325	0.46
24	80.137	80.053	−0.10
25	85.696	86.072	0.44
26	88.859	88.871	0.01
27	89.319	89.379	0.07
28	90.513	90.876	0.40
29	93.144	93.525	0.41
30	—	95.089	—
31	97.005	97.398	0.41
32	—	98.160	—
33	101.130	101.375	0.24
34	102.220	102.419	0.19

6.6 Sample 2: Layer Width of 36.79 nm

Table 6.6: Resonances frequencies from Sample 2 are presented in kHz.

	Measurement	Estimated Resonance Frequency				
Mode	Position 1	Position 1	Position 2	Position 3	Position 4	Position 5
21	14.917	14.89	14.91	14.82	14.83	14.89
22	14.980	14.98	—	—	—	15.01
25	18.401	18.39	18.32	18.37	18.31	—
26	18.816	18.79	18.78	18.68	18.73	18.82
28	20.433	20.43	20.47	20.42	20.46	20.47
31	23.331	23.33	22.94	23.09	22.90	23.11
32	—	—	23.63	—	23.57	23.59
35	26.236	26.26	26.26	26.20	26.24	26.31
38	28.310	28.27	28.25	28.20	28.17	28.33
39	28.755	28.75	—	—	—	28.81
40	29.855	29.80	31.05	29.63	30.42	30.68
42	31.116	31.11	31.19	31.11	31.12	31.13
43	32.141	32.14	—	32.12	32.19	32.20
44	32.900	32.91	32.90	—	32.89	32.90
45	34.436	34.42	—	34.42	34.40	34.39
46	34.968	34.98	34.83	34.74	34.73	34.92
47	35.553	35.55	—	35.55	35.59	35.60
48	37.017	37.00	36.91	36.90	—	36.96
49	37.846	37.85	37.88	37.77	37.85	37.91
50	40.122	40.10	40.10	40.00	40.06	40.13
52	42.226	42.19	42.05	42.02	42.00	42.18
55	43.905	43.85	43.86	43.62	43.71	43.90
56	—	—	44.98	—	44.96	44.95
57	—	46.27	—	—	46.30	46.33
61	50.080	49.93	50.42	49.96	50.31	50.42
64	53.446	53.44	53.55	53.43	53.51	53.52
65	54.304	54.29	54.31	54.29	54.29	54.30
67	56.288	56.27	56.38	56.23	56.25	56.38
69	60.412	60.40	—	60.24	60.30	60.45
70	60.545	60.53	60.52	—	—	—
71	61.681	61.61	61.67	61.55	61.59	61.69
72	63.138	63.05	63.11	62.96	63.05	63.15
74	64.464	64.45	64.52	64.47	64.45	64.49
78	66.651	66.65	—	—	—	—
79	67.688	67.63	67.17	—	67.10	67.26
83	70.883	70.88	—	70.73	—	70.97
84	72.269	72.28	72.41	—	72.21	72.42
85	—	73.59	—	73.51	73.67	73.70
86	75.809	75.83	75.94	75.81	75.91	75.96
87	76.501	76.51	—	—	76.68	—
88	78.598	78.61	—	—	—	—
90	81.272	81.27	—	81.22	—	—
91	81.987	81.99	82.22	—	82.13	82.14
93	85.666	85.64	86.26	—	86.11	86.11
94	87.870	87.90	—	—	—	—
95	—	89.42	89.35	89.29	89.25	89.35
98	—	90.49	90.77	—	90.67	90.71
100	92.915	92.95	92.88	92.81	92.77	92.89
103	—	95.85	95.96	—	95.90	95.95
104	100.666	100.70	—	—	—	100.60
105	101.147	101.10	101.30	—	101.20	101.30
106	102.384	102.40	—	—	—	—

For sample 2, the length is larger than sample 1 while the width and thickness are smaller. This causes sample 2 to have a larger amount of resonances under 15 kHz. This produces a greater uncertainty as our measurements start with higher mode numbers. We present our measurements and estimates from different positions of the sample in Table 6.6. We measured 45 resonance frequencies.

We attempted at least 72 fits using cubic symmetry and we present a portion of them in Table 6.7. Fit 1 was started at the estimates of the effective elastic constants. Fit 2 was started near the fit parameters of sample 1. Fits 3 through 6 were started at points that were identified as minima of sample 2 either in the parameter space search or in a prior fitting routine we conducted. Similarly, Fits 7 and 8 were started at points that were identified as minima of sample 3 either in the parameter space search or in a prior fitting routine we conducted. Fit 9 was set to start near the center of the parameter space search.

Table 6.7: A portion of the fits that were performed with sample 2 are presented. Fits were performed using rpr.exe with $N = 19$ and all fits presented took 30 iterations. Fits 5 and 6 had the same mode identification. Fit 3 failed to converge.

Fit	Highest Mode Number	Label	C_{11}	C_{12}	C_{44}	RMS
1	63	Initial	2.08	1.21	0.43	3.9206 %
		Final	2.0 ± 0.2	1.1 ± 0.2	0.42 ± 0.02	3.441 %
2	65	Initial	1.6373	0.7750	0.38920	3.8887 %
		Final	1.45 ± 0.07	0.63 ± 0.09	0.42 ± 0.01	3.1352 %
3	128	Initial	1.6240	1.5621	0.3169	1.0673 %
		Final	—	—	—	—
4	65	Initial	2.24	1.42	0.4766	7.4794 %
		Final	2.15 ± 0.05	1.43 ± 0.05	0.39 ± 0.01	3.184 %
5	65	Initial	2.04	1.26	0.45	4.9456 %
		Final	1.68 ± 0.04	0.93 ± 0.04	0.42 ± 0.01	2.9164 %
6	65	Initial	2.10	1.35	0.39	3.1939 %
		Final	1.75 ± 0.07	1.00 ± 0.08	0.40 ± 0.01	2.9235 %
7	91	Initial	1.80	1.41	0.30	18.6934 %
		Final	1.75 ± 0.04	1.48 ± 0.04	0.219 ± 0.007	3.0701 %
8	106	Initial	1.5756	1.4583	0.2884	1.2377 %
		Final	1.2 ± 0.3	1.1 ± 0.3	0.299 ± 0.002	1.0987 %
9	62	Initial	2.20	1.20	0.43	6.9056 %
		Final	2.6 ± 0.1	1.8 ± 0.1	0.41 ± 0.02	3.784 %

For each of these starting points, a mode identification was performed. Because 2 of these fits had the same mode identification, there were 8 independent mode identifications. We then tested the 8x9=72 combinations of these distinct mode identifications with these sets of starting parameters. Of all of these fits, the one that produced the smallest rms error was the labeled fit 8. However, the uncertainties on certain parameters from other fits with higher rms errors were lower. This can also be observed in Table 6.7. This illustrates the point that Migliori makes in [8], where he explains that the rms error does not characterize the accuracy of a fit.

The fits we performed in Table 6.7 took 30 iterations, which is the maximum amount allowed by rpr.exe before the code stops. This suggests that the fits themselves were not very stable. The majority of our fits provided different results for the parameters although the rms errors were comparable in some cases. This is evidence that the objective function we are trying to minimize has multiple minima. Because of this, we consider the uncertainties of our measurements in sample 2 to be too large to successfully determine the elastic constants. We show the resonance frequencies of Fit 8 from sample 2 in Table 6.8 and we present a graphical representation in Fig. 6-2. However, this data is not sufficient to characterize sample 2.

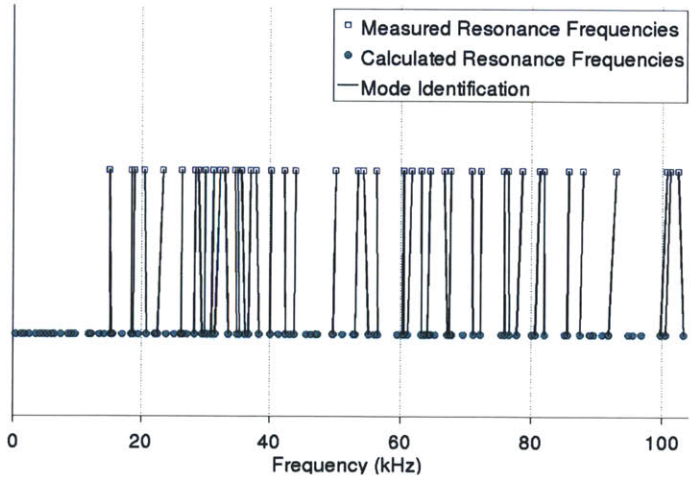

Figure 6-2: The measured resonances of sample 2 along with the calculated resonances of the fit parameters and their mode identifications are presented.

Table 6.8: The results from fit 8 of sample 2 are presented. The input parameters were $C_{11} = 1.2$, $C_{12} = 1.1$, and $C_{44} = 0.299$. The rms error was 1.0987%.

Mode	Measured Freq.	Calculated Freq.	% Error
21	14.917	15.125	1.39
22	14.980	15.228	1.66
25	18.401	18.402	0.01
26	18.816	18.687	−0.68
28	20.433	20.756	1.58
31	23.331	22.464	−3.72
35	26.236	26.134	−0.39
38	28.310	28.184	−0.44
39	28.754	29.340	2.04
40	29.855	29.814	−0.14
42	31.116	30.823	−0.94
43	32.141	31.350	−2.46
44	32.900	33.449	1.67
45	34.436	34.771	0.97
46	34.968	35.291	0.92
47	35.553	36.204	1.83
48	37.017	36.736	−0.76
49	37.846	38.340	1.31
50	40.122	40.067	−0.14
52	42.226	42.423	0.47
55	43.905	43.771	−0.30
61	50.080	49.702	−0.76
64	53.446	53.062	−0.72
65	54.304	55.087	1.44
67	56.288	56.544	0.45
69	60.412	60.310	−0.17
70	60.545	60.504	−0.07
71	61.680	61.127	−0.90
72	63.138	63.205	0.11
74	64.464	64.114	−0.54
78	66.651	67.168	0.78
79	67.688	67.482	−0.30
83	70.883	71.136	0.36
84	72.269	72.256	−0.02
86	75.810	75.947	0.18
87	76.501	76.640	0.18
88	78.598	77.790	−1.03
90	81.272	80.614	−0.81
91	81.987	82.005	0.02
93	85.666	85.499	−0.19
94	87.870	87.458	−0.47
100	92.915	91.827	−1.17
104	100.670	99.686	−0.98
105	101.150	100.494	−0.65
106	102.380	103.235	0.83

6.7 Sample 3: Layer Width of 16.78 nm

Table 6.9: Resonances frequencies from Sample 3 are presented in kHz.

	Measurement	Estimated Resonance Frequency				
Mode	Position 1	Position 1	Position 2	Position 3	Position 4	Position 5
20	14.507	14.51	—	—	14.46	—
21	15.242	15.24	15.14	15.07	15.11	14.91
23	16.373	16.37	—	16.37	16.38	—
25	18.992	19.01	18.72	18.71	18.91	18.63
26	19.655	19.63	19.54	19.56	19.58	19.41
28	22.222	22.19	22.14	22.14	22.20	22.08
31	24.162	24.09	23.72	23.68	23.96	23.61
33	24.867	24.85	24.82	24.84	24.83	24.66
36	—	27.50	27.46	27.46	27.48	27.43
38	28.233	28.23	28.26	28.26	28.28	28.20
39	30.398	30.36	30.21	30.18	30.30	30.11
40	30.870	30.87	30.85	30.84	30.84	30.77
41	32.076	32.05	31.93	31.93	32.03	31.89
42	32.959	32.95	32.83	32.81	32.86	32.71
44	34.356	34.37	34.40	34.33	34.36	34.38
45	34.638	34.62	34.60	34.60	34.65	34.54
46	35.797	35.80	—	—	36.44	35.19
47	37.008	36.96	36.77	36.74	36.93	36.65
48	39.232	39.16	38.71	38.68	38.98	38.34
49	39.972	39.93	—	—	39.90	—
50	—	40.39	—	—	40.44	—
55	44.311	44.28	44.12	44.07	44.24	43.97
56	45.550	45.48	45.05	45.03	45.34	—
58	47.564	47.56	47.65	47.64	47.66	—
60	49.361	49.36	49.23	49.21	49.26	49.15
61	51.643	51.60	51.28	51.29	51.49	51.01
62	52.608	52.58	52.60	52.56	—	—
64	55.653	55.67	55.68	55.67	—	55.57
65	—	—	56.19	56.19	—	—
66	57.425	57.44	57.33	57.32	—	57.25
67	59.642	—	59.27	59.27	—	59.10
70	—	—	60.79	60.77	—	—
71	61.549	61.56	61.64	61.62	—	61.42
72	62.046	62.05	62.05	62.10	—	61.56
76	65.300	65.23	64.99	64.97	—	64.81
77	66.156	66.18	66.15	66.14	—	—
78	66.525	66.53	—	—	—	—
79	69.248	69.24	69.14	69.14	—	68.93
80	—	—	69.74	69.83	—	69.14
81	71.048	71.04	70.85	70.82	—	70.50
84	—	—	74.62	74.67	—	74.30
86	76.931	76.93	77.01	77.02	—	76.95
87	78.412	78.43	78.45	78.47	—	78.36
88	—	—	79.66	79.63	—	79.45
91	82.733	82.69	82.59	82.60	—	81.99
94	—	85.61	—	85.63	—	85.63
97	89.517	89.60	89.37	89.37	—	89.22
98	—	90.58	90.56	90.61	—	90.45
99	—	93.43	93.19	93.19	—	93.09
100	94.402	94.41	—	—	—	94.25
102	96.170	96.18	96.02	96.00	—	95.78
103	97.137	97.13	—	—	—	96.86

For sample 3, the geometry is similar to that of sample 2. As a result, it also has a large amount of resonances under 15 kHz. We present our measurements and estimates from different positions of the sample in Table 6.9. We measured 42 resonances.

We attempted at least 45 fits using cubic symmetry and we present a portion of them in Table 6.10. Fit 1 through 9 were performed using the same starting parameters as with sample 2. For each of these starting parameters, a mode identification was performed with our set of measured resonances. Several of these fits had the same mode identification. As a result, there were a total of 5 independent mode identifications. We then tested the 5x9=45 combinations of these distinct mode identifications with these sets of starting parameters. Of all of these fits, the one that produced the smallest rms error was the labeled fit 8. It is interesting that this is the same as what occured with sample 2. However, the uncertainties parameters from other fits with higher rms errors were lower, as can be observed in Table 6.10.

Table 6.10: A portion of the fits that were performed with sample 3 are presented. Fits were performed using rpr.exe with $N = 19$ and all fits presented took 30 iterations. Fits 1 and 9 had the same mode identification. Fits 2, 4, 5 and 6 had the same mode identification.

Fit	Highest Mode Number	Label	C_{11}	C_{12}	C_{44}	RMS
1	61	Initial	2.08	1.21	0.43	5.5292 %
		Final	2.0 ± 0.3	1.1 ± 0.4	0.39 ± 0.02	4.4033 %
2	62	Initial	1.6373	0.7750	0.38920	4.6344 %
		Final	1.7 ± 0.2	0.8 ± 0.2	0.34 ± 0.01	3.3180 %
3	118	Initial	1.6240	1.5621	0.3169	1.5961 %
		Final	3.2 ± 6.4	3.1 ± 6.5	0.310 ± 0.003	1.5438 %
4	62	Initial	2.24	1.42	0.4766	8.7632 %
		Final	2.3 ± 0.1	1.7 ± 0.1	0.39 ± 0.02	3.5778 %
5	62	Initial	2.04	1.26	0.45	6.0549 %
		Final	2.1 ± 0.2	1.4 ± 0.2	0.38 ± 0.02	3.5748 %
6	62	Initial	2.10	1.35	0.39	4.0584 %
		Final	2.1 ± 0.2	1.4 ± 0.2	0.37 ± 0.02	3.5747 %
7	87	Initial	1.80	1.41	0.30	20.2514 %
		Final	1.73 ± 0.01	1.47 ± 0.01	0.215 ± 0.007	3.1779 %
8	103	Initial	1.5756	1.4583	0.2884	1.2260 %
		Final	1.6 ± 0.9	1.5 ± 0.9	0.287 ± 0.002	1.2198 %
9	61	Initial	2.20	1.20	0.43	9.0596 %
		Final	1.9 ± 0.2	1.1 ± 0.3	0.38 ± 0.02	4.4102 %

The fits we performed in Table 6.10 also took 30 iterations, suggesting that the fits themselves were not very stable. The majority of our fits provided different results for the parameters although the rms errors were comparable in some cases. This is evidence that the objective function for sample 3 also has multiple minima. Because of this, we consider the uncertainties of our measurements in sample 3 to be too large to successfully determine the elastic constants. We show the resonance frequencies of Fit 8 from sample 3 in Table 6.11 and we present a graphical representation in Fig. 6-3. However, this data is not sufficient to characterize sample 3.

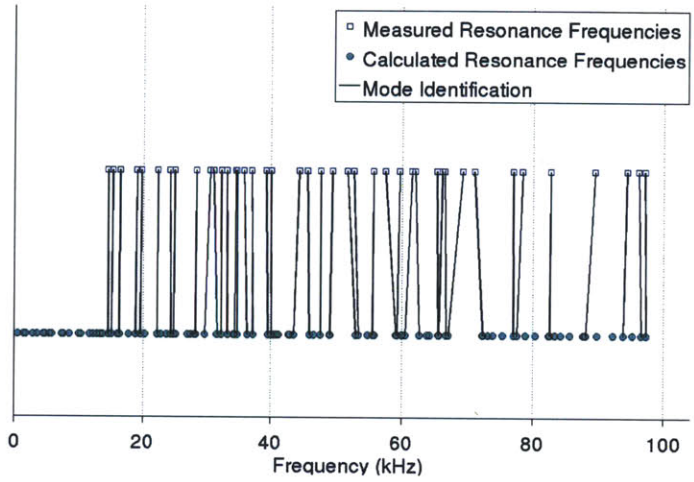

Figure 6-3: The measured resonance frequencies of sample 3 along with the calculated resonances of the fit parameters and their mode identifications are presented.

Table 6.11: The results from fit 8 of sample 3 are presented. The input parameters were $C_{11} = 1.6$, $C_{12} = 1.5$, and $C_{44} = 0.287$. The rms error was 1.2198%.

Mode	Measured Freq.	Calculated Freq.	% Error
20	14.507	14.575	0.47
21	15.242	15.111	−0.86
23	16.373	16.292	−0.49
25	18.992	18.786	−1.09
26	19.655	19.525	−0.66
28	22.222	22.177	−0.20
31	24.162	24.283	0.50
33	24.867	24.746	−0.49
38	28.233	28.104	−0.46
39	30.398	29.565	−2.74
40	30.870	31.476	1.96
41	32.076	32.114	0.12
42	32.959	33.074	0.35
44	34.356	34.206	−0.44
45	34.638	34.673	0.10
46	35.797	36.339	1.51
47	37.008	37.220	0.57
48	39.232	39.575	0.87
49	39.972	40.109	0.34
55	44.311	43.522	−1.78
56	45.550	45.860	0.68
58	47.564	47.591	0.06
60	49.361	49.020	−0.69
61	51.643	52.919	2.47
62	52.608	53.408	1.52
64	55.653	55.517	−0.24
66	57.425	59.133	2.98
67	59.642	59.287	−0.59
71	61.549	60.548	−1.63
72	62.046	62.697	1.05
76	65.300	65.557	0.39
77	66.156	65.693	−0.70
78	66.525	66.756	0.35
79	69.248	67.081	−3.13
81	71.048	72.364	1.85
86	76.931	77.030	0.13
87	78.412	77.568	−1.08
91	82.733	82.599	−0.16
97	89.517	88.130	−1.55
100	94.402	93.846	−0.59
102	96.170	96.589	0.44
103	97.137	97.351	0.22

6.8 Summary of Results

We performed measurements of resonance frequencies for the three samples. However, we consider only our fits for the elastic constants of sample 1 to have been successful. For samples 2 and 3 the uncertainties on the parameters themselves were too large, and we believe this to be a result of the existence of multiple minima in the objective function that we are trying to minimize. We present the fit results with the lowest rms errors from the three samples in Table 6.12.

Although our fits from samples 2 and 3 weren't successful. An interesting feature of our results is that the average rms error from our fits increased with increasing interface area-to-volume ratio. This shows that there are greater uncertainties in our RUS measurements with decreasing layer width. This could provide indirect evidence that there is a third component, aside from the copper and niobium layers, and it has an increasingly important role as the layer width decreases. This third component can be considered the interfaces between successive copper and niobium layers. Although our measurements do not have sufficient accuracy to determine the properties of the interfaces, our data could provide some evidence of the greater influence these interfaces have on the elastic constants of the composite at smaller layer widths.

Table 6.12: The fit results for the three samples are presented together.

	Sample 1	Sample 2	Sample 3
C_{11}	1.63 ± 0.02	1.2 ± 0.3	1.6 ± 0.9
C_{22}	1.63 ± 0.02	1.2 ± 0.3	1.6 ± 0.9
C_{33}	1.63 ± 0.02	1.2 ± 0.3	1.6 ± 0.9
C_{23}	0.77 ± 0.03	1.1 ± 0.3	1.5 ± 0.9
C_{13}	0.77 ± 0.03	1.1 ± 0.3	1.5 ± 0.9
C_{12}	0.77 ± 0.03	1.1 ± 0.3	1.5 ± 0.9
C_{44}	0.389 ± 0.002	0.299 ± 0.002	0.287 ± 0.002
C_{55}	0.389 ± 0.002	0.299 ± 0.002	0.287 ± 0.002
C_{66}	0.389 ± 0.002	0.299 ± 0.002	0.287 ± 0.002
RMS Error	0.575 %	1.0987 %	1.2198 %

Chapter 7

Conclusions

In our research with the Cu/Nb composites, we did not achieve successful measurements of elastic properties of all of our samples. Because of this, we were unable to reach our goal of characterizing the properties of the interfaces. However, the problems we encountered allowed us to identify several sources of uncertainty, paving the way for improved measurements in the future.

We successfully simulated the convergence behaviors of the direct code using different baseses for displacement fields. This work provided evidence that homogenized elastic constants may be used to compute resonance frequencies in certain layered composites. We developed a numerical approach to mode identification. We also performed a texture analysis in order to develop starting values for the elastic constants in the fitting routines. These developments can help obtain a successful measurement of the elastic constants.

We started by developing codes that implement both the linear Lagrange interpolation basis and the power series basis in Chapter 3. Both of these codes were implemented prior to our work. However, to our knowledge, there had not been simulations about the convergence behaviors for composites. We conducted simulations, which showed that when the power serics basis is implemented with a layered composite, the resonance frequencies approach those of a homogeneous system whose elastic constants are the arithmetic mean of its constituents. This contradicts well-known analytical results from composite homogenization theory. When the interpolation basis

is implemented instead, the resonance frequencies approach those of a homogeneous system whose elastic constants are consistent with composite homogenization theory. This finding also shows that homogenized elastic constants can be implemented in RUS with certain composite systems.

At the experimental level, we have found evidence of the limitations of RUS with accumulated roll bonded samples near 7 nm (sample 4). At that stage, the ARB process can lead to fracturing of the material, which increases the inhomogeneities in the material and impedes successful measurements.

Given that we did not have prior knowledge about the actual elastic constants of the Cu/Nb composites, we had problems with the procedure of conducting a mode identification. To help with this process, we developed a numerical algorithm in Chapter 4 to perform the mode identification for us. This approach is limited as it cannot test all combinations of mode identifications. Improved mode identification would be possible if not only the resonance frequencies, but also the resonance shapes were measured in RUS experiments.

We performed measurements with three Cu/Nb composites. Only in the case of sample 1 do we consider our measurements to have been successful. From our attempts to perform fits of the elastic constants in samples 2 and 3, we have found that the objective function has multiple minima that have impeded us from successfully determining the elastic properties of the composite. There were marked divergences in the elastic constants from fits with comparable errors. We implemented a texture analysis in Chapter 6 to try to improve our starting parameters using the self-consistent method of Tomé[22] to calculate polycrystalline elastic constants for Cu and Nb assuming a random texture. We then homogenized the composite by calculating the effective elastic constants and we used those as starting parameters. Aside from that, we also did a parameter space search. Nevertheless, the uncertainties were too large in samples 2 and 3. However, we have found that our data showed increasing uncertainties and rms errors with decreasing layer widths.

In order to achieve a successful measurement of the elastic properties of samples 2 and 3, several improvements to RUS should be made. The framework developed by

Tomé could be expanded to consider cases in layered composites where the layers have only one or two grains across their thickness. This could provide a better estimate of starting parameters for the fitting procedure. Another option would be to model the mode shapes using the eigenvectors of the direct code as Ogi and coworkers have done.[21] Although, it is not numerically feasible to implement the interpolation basis at very small layer widths, it could be investigated if the eigenvectors have the same convergence behavior as their eigenvalues. If such is the case, the homogeneous codes prepared by Ogi and Heyliger could be used to achieve a successful mode identification of the layered composites at smaller layer widths. Such advancements could allow for successful measurements of the elastic properties of the Cu/Nb composites.

Bibliography

[1] A Fartash, Eric E Fullerton, Ivan K Schuller, Sarah E Bobbin, JW Wagner, RC Cammarata, Sudha Kumar, and M Grimsditch. Evidence for the supermodulus effect and enhanced hardness in metallic superlattices. *Physical Review B*, 44(24):13760, 1991.

[2] SB Lee, JE LeDonne, SCV Lim, IJ Beyerlein, and AD Rollett. The heterophase interface character distribution (hicd) of physical vapor-deposited and accumulative roll-bonded cu-nb multilayer composites.

[3] MJ Demkowicz and RG Hoagland. Simulations of collision cascades in cu–nb layered composites using an eam interatomic potential. *International Journal of Applied Mechanics*, 1(03):421–442, 2009.

[4] Keith J Bowman. *Mechanical behavior of materials*, volume 1. Wiley New York, 2004.

[5] Albert Migliori and John L Sarrao. *Resonant ultrasound spectroscopy.* Wiley New York, 1997.

[6] A Migliori, JL Sarrao, William M Visscher, TM Bell, Ming Lei, Z Fisk, and RG Leisure. Resonant ultrasound spectroscopic techniques for measurement of the elastic moduli of solids. *Physica B: Condensed Matter*, 183(1):1–24, 1993.

[7] A. Migliori et al. *Resonant Ultrasound Spectroscopy (RUS)*, volume 39 of *Modern Acoustical Techniques for the Measurement of Mechanical Properties.* Academic Press, 2001.

[8] Albert Migliori and JD Maynard. Implementation of a modern resonant ultrasound spectroscopy system for the measurement of the elastic moduli of small solid specimens. *Review of scientific instruments*, 76(12):121301–121301, 2005.

[9] LAPACK (April 2011) *DSYGV* (Version 3.3.1) [Software]. Available from: http://www.netlib.org/lapack/double/dsygv.f.

[10] A. Migliori and W. M. Visscher et al. *J. Acoust. Soc. Am.*, 90(4), 1991.

[11] P. Heyliger. Traction-free vibration of layered elastic and piezoelectric rectangular parallelepipeds. *J. Acoust. Soc. Am.*, 107(3):1235+, March 2000.

[12] P. Heyliger et. al. Elastic constants of layers in isotropic laminates. *J. Acoust. Soc. Am.*, 114(5):2618+, November 2003.

[13] Hirotsugu Ogi, Paul Heyliger, Hassel Ledbetter, and Sudook Kim. Mode-selective resonance ultrasound spectroscopy of a layered parallelepiped. *The Journal of the Acoustical Society of America*, 108:2829, 2000.

[14] J. N. Reddy. *Communications in Applied Numerical Methods*, 3:173–180, 1987.

[15] J. N. Reddy. *An Introduction to the Finite Element Method.* McGraw-Hill, 3rd edition, 2006.

[16] Albert Migliori (2006) *rpr.exe* (Version 6.0) [Computer Program]. Available from: http://www.magnet.fsu.edu/inhouseresearch/rus/index.html.

[17] María Teresa Cerda Guevara. Estudio sobre la densidad de dislocaciones y constantes elásticas en aluminio policristalino mediante espectroscopía de resonancia ultrasónica. Master's thesis, University of Chile, 2009.

[18] I. Ohno. *J. Phys. Earth*, 24:355–379, 1976.

[19] M. Grimsditch. *American Physical Society*, 31(10), 1985.

[20] HPR Frederikse. Elastic constants of single crystals. *CRC Handbook*, pages 33–38, 2008.

[21] Hirotsugu Ogi, Keiji Sato, Takeyasu Asada, and Masahiko Hirao. Complete mode identification for resonance ultrasound spectroscopy. *The Journal of the Acoustical Society of America*, 112:2553, 2002.

[22] U Fred Kocks, Carlos Norberto Tomé, and H-R Wenk. *Texture and anisotropy: preferred orientations in polycrystals and their effect on materials properties.* Cambridge university press, 2000.